Upstream Sources of the Denmark Strait Overflow: Observations from a High-Resolution Mooring Array

B. E. Harden[a,*], R. S. Pickart[a], Héðinn Valdimarsson[b], Kjetil Våge[c], Laura deSteur[d,e], Clark Richards[a], Frank Bahr[a], Dan Torres[a], Eli Børve[c,h], Steingrímur Jónsson[b,f], Andreas Macrander[b], Svein Østerhus[g], Lisbeth Håvik[c], Tore Hattermann[h]

[a]*Woods Hole Oceanographic Institution, Woods Hole, USA*
[b]*Marine Research Institute, Reykjavik, Iceland*
[c]*Geophysical Institute and Bjerknes Centre for Climate Research, University of Bergen, Norway*
[d]*Royal Netherlands Institute for Sea Research NIOZ, Texel, The Netherlands*
[e]*Norwegian Polar Institute, Tromsø, Norway*
[f]*University of Akureyri, Iceland*
[g]*Uni Reseach Climate, Bergen, Norway*
[h]*Akvaplan-niva, Tromsø, Norway*

Abstract

We present the first results from a densely instrumented mooring array upstream of the Denmark Strait sill, extending from the Iceland shelfbreak to the Greenland shelf. The array was deployed from September 2011 to July 2012, and captured the vast majority of overflow water denser than 27.8 kg m^{-3} approaching the sill. The mean transport of overflow water over the length of the deployment was 3.54 $\pm$ 0.16 Sv. Of this, 0.58 Sv originated from below sill depth, revealing that aspiration takes place in Denmark Strait. We confirm the presence of two main sources of overflow water: one approaching the sill in the East Greenland Current and the other via the North Icelandic Jet. Using an objective technique based on the hydrographic properties of the water, the transports of these two sources are found to be 2.54 $\pm$ 0.17 Sv and 1.00 $\pm$ 0.17 Sv, respectively. We further partition the East Greenland Current source into that carried by the shelfbreak jet (1.50 $\pm$ 0.16 Sv) versus that transported by a separated branch of the current on the Iceland slope (1.04 $\pm$ 0.15 Sv). Over the course of the year the total overflow transport

*Corresponding author.
Email address: bharden@whoi.edu (B. E. Harden)

is more consistent than the transport in either branch; compensation takes place among the pathways that maintains a stable total overflow transport. This is especially true for the two East Greenland Current branches whose transports vary out of phase with each other on weekly and longer time scales. We argue that wind forcing plays a role in this partitioning.
Keywords:

---

1. Introduction

The Nordic Seas are a vital region for the circulation of the North Atlantic and the maintenance of our climate. Warm, sub-tropical waters flowing northward into the Nordic Seas are modified by intense air-sea fluxes and release heat to the atmosphere before returning south as dense waters that spill over the ridge between Greenland and Scotland. This process regulates our climate by transporting heat northward in the Atlantic Ocean. The largest and ultimately the densest of the outflows occurs through the Denmark Strait, located between Iceland and Greenland (sill depth of 650 m, see Figure 1), which accounts for roughly half of the total dense water feeding the Deep Western Boundary Current (Dickson and Brown, 1994). However, there remain significant gaps in our knowledge of where the Denmark Strait Overflow Water (DSOW) originates from and how the circulation upstream of the ridge affects the dynamics of the overflow.

Early studies focused on open-ocean convection in the Iceland and Greenland Seas as the main sources of DSOW (Swift et al., 1980; Swift and Aagaard, 1981; Smethie and Swift, 1989; Strass et al., 1993). However, Mauritzen (1996) subsequently argued that the primary source was not the interior basins, but rather the Nordic Seas boundary current system. In particular, Mauritzen (1996) demonstrated that the warm, surface Norwegian Atlantic Current inflow progressively cools as it flows around the perimeter of the Nordic Seas (with a branch circulating within the Arctic Ocean). It then exits as

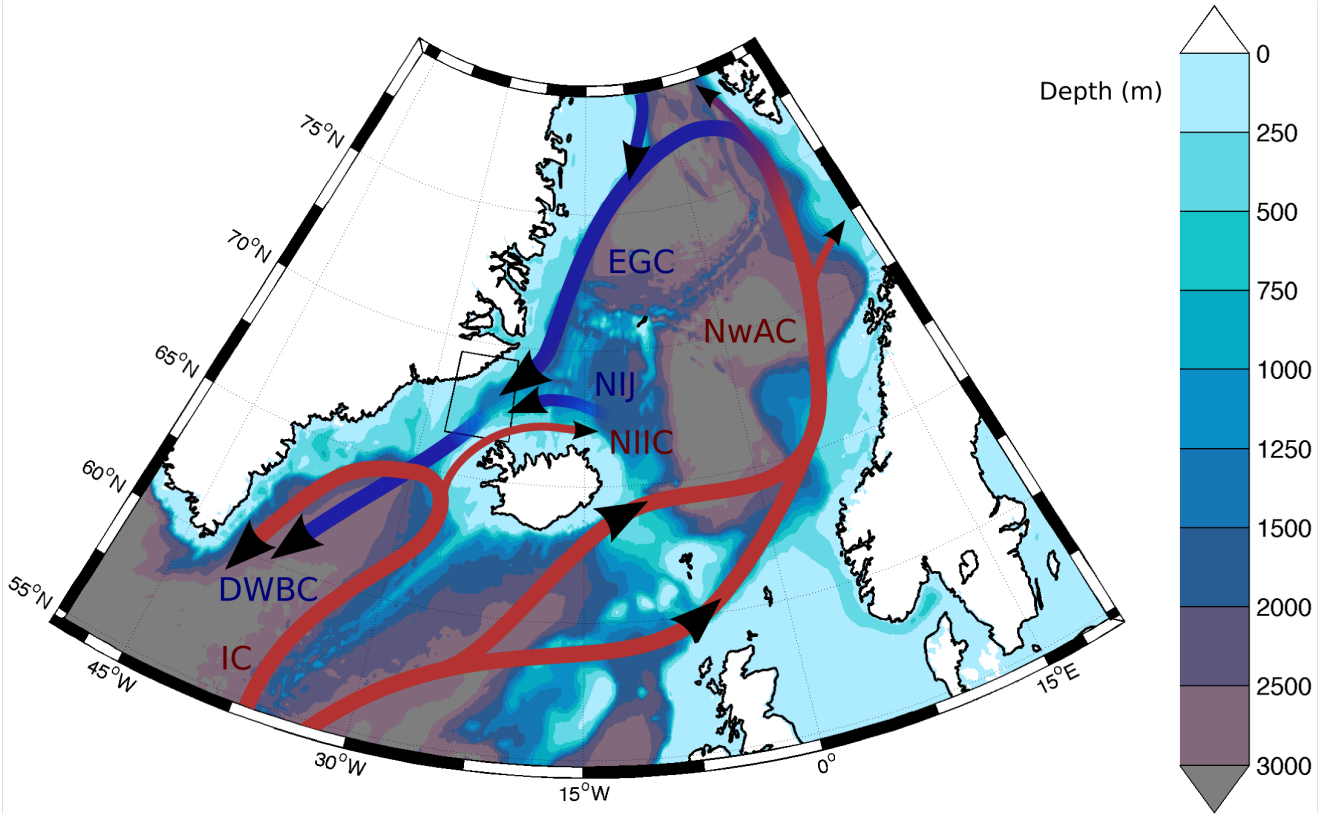

Figure 1: Schematic of the major currents pertinent to this study, north and south of Iceland. Shown in red are the warm surface currents: the Norwegian Atlantic Current (NwAC), the Irminger Current (IC), and the North Icelandic Irminger Current (NIIC). Shown in blue are dense water pathways: the Deep Western Boundary Current (DWBC), fed by the Denmark Strait Overflow, the East Greenland Current (EGC), and the North Icelandic Jet (NIJ). The bathymetry is from ETOPO5. The study region in the Denmark Strait is shown with the black box (see Figure 3).

dense, salty overflow water in the East Greenland Current (EGC), approaching the Denmark Strait along the Greenland continental slope and shelfbreak (Figure 1). The notion that the EGC was the primary conduit for bringing overflow water into Denmark Strait was further supported through hydrographic measurements (Rudels et al., 2002), historical data (Eldevik et al., 2009), tracer studies (Tanhua et al., 2005), and high-resolution numerical modeling (Köhl et al., 2007).

Roughly a decade after Mauritzen (1996)'s study, however, Jónsson and Valdimarsson (2004) pro-

posed a second significant source of DSOW that approaches the strait from the Iceland Slope. Using shipboard velocity measurements they discovered a deep-reaching current transporting water dense enough to contribute to the overflow. Additional field studies have since confirmed the existence of this equatorward current, now known as the North Icelandic Jet (NIJ), which is thought to be distinct from the EGC and to carry the densest third of the overflow water to the Denmark Strait sill (Våge et al., 2011b, 2013). Våge et al. (2011b) further hypothesized that the NIJ is the lower limb of a local overturning cell in the Iceland Sea. In their model, the northward flowing North Icelandic Irminger Current (NIIC) constitutes the upper limb of the cell which transports warm, subtropical-origin water into the Iceland Sea. The current then sheds the warm water into the interior basin via eddies, which are densified by convection during winter. Ultimately the dense water returns westward to the slope, sinks, and forms the NIJ, thus completing the overturning loop (Figure 2). This proposed mechanism has served to refocus attention in the community back to the interior basins as a possible source of overflow water.

The circulation in the region upstream of Denmark Strait was further elucidated by Våge et al. (2013) who identified yet a third possible pathway of overflow water to the sill: a free-jet located between the Shelfbreak EGC and the NIJ. They called this feature the Separated EGC due to their assertion that it bifurcates from the Shelfbreak EGC upstream of the Strait. Using a combination of in-situ observations and modeling, Våge et al. (2013) argued that the baroclinically unstable current at the shelfbreak sheds eddies that propagate across the Blosseville Basin north of the Denmark Strait and coalesce on the deep Iceland slope to form the semi-permanent separated EGC. Their complete upstream circulation scheme, including the hypothesized NIJ overturning cell, is shown in Figure 2.

The recent discoveries of multiple sources and pathways of dense water to the Denmark Strait has reinforced the fact that we still lack a complete understanding of the formation processes and dynamics

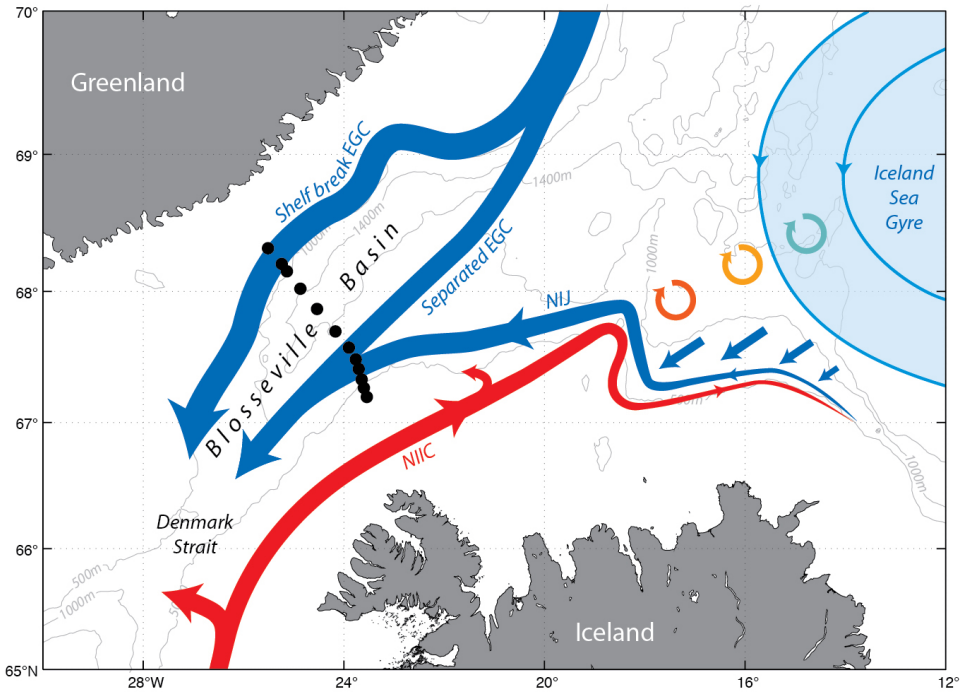

Figure 2: Schematic circulation in the region of the Blosseville Basin, upstream of the Denmark Strait sill, as proposed by Våge et al. (2011b) and Våge et al. (2013). Shown in blue are the three proposed pathways of overflow water to the sill: the Shelfbreak East Greenland Current (Shelfbreak EGC), Separated EGC, and North Icelandic Jet (NIJ). Våge et al. (2013) calculated transports of 0.8 $\pm$ 0.3 Sv, 1.3 $\pm$ 0.4 Sv, and 1.4 $\pm$ 0.3 Sv respectively for the three branches from four synoptic crossings of the current system. The overturning cell proposed by Våge et al. (2011b) is also shown (see the text for a description of the cell). The locations of the moorings in the Kögur array are indicated by the black dots.

that supply DSOW to the sill. This in turn makes it difficult to predict how the Atlantic Meridional Overturning Circulation (AMOC) will respond to changes in freshwater sources and spreading patterns, shifting sea ice distributions, or changing atmospheric conditions in the Nordic Seas. Determining the nature and quantity of each dense water source, their upstream dynamics, and the factors that dictate the full transport at the sill is vital for assessing how robust the dense water export is from the Nordic Seas and, correspondingly, how effectively heat can be transported poleward in the North Atlantic.

Until now we have been reliant on a limited number of synoptic sections across the Denmark Strait and Blosseville Basin (mostly occupied during the summer months) to describe the relative importance of the dense water branches. Past moored measurements have been geographically limited, and the historical data from the region typically lack velocity measurements for transport estimates. As such, fundamental questions exist regarding the circulation upstream of the sill. For instance, are the NIJ and Separated EGC consistent, year-round contributors to the overflow? If so, how do these two branches, as well as the the Shelfbreak EGC, vary through the year? Since the DSOW transport at the sill displays no significant seasonal cycle (Jochumsen et al., 2012), does this mean that the three pathways continually compensate each other? Våge et al. (2013) produced transport estimates for the separate pathways, but observed significant section-to-section variability, highlighting how little we know about the time-variation of each branch and the mechanisms behind these fluctuations.

In this paper we seek to fundamentally improve our understanding of the upstream sources and pathways of dense water into the Denmark Strait overflow. We present results from a densely instrumented mooring array deployed upstream of the sill for 11 months from 29 Aug 2011 to 30 July 2012. The array spanned the Blosseville Basin from the Iceland shelfbreak to the Greenland shelf, and hence captured, for the first time, the complete overflow transport towards the sill. We describe the velocity structure and water mass characteristics of the upstream circulation, elucidating the nature of each branch. We then calculate the total overflow transport and partition this between the three pathways. Finally, we examine the wind-driven partitioning between the sources, with specific focus on the transport division between the two East Greenland Current branches.

2. Data and Methods

The mooring array considered here was deployed across the Blosseville Basin upstream of the Denmark Strait sill for 11 months from 29 Aug 2011 to 30 July 2012 along the previously established Kögur line (Figure 3). The array is thus referred to as the Kögur array. Each of the 12 moorings (denoted as KGA1–KGA12, starting from the southeastern-most site) was equipped with an assortment of instruments measuring temperature, salinity, pressure, and current velocity. A full inventory of the recovered instrumentation is shown diagrammatically in Figure 4, and can be described as follows.

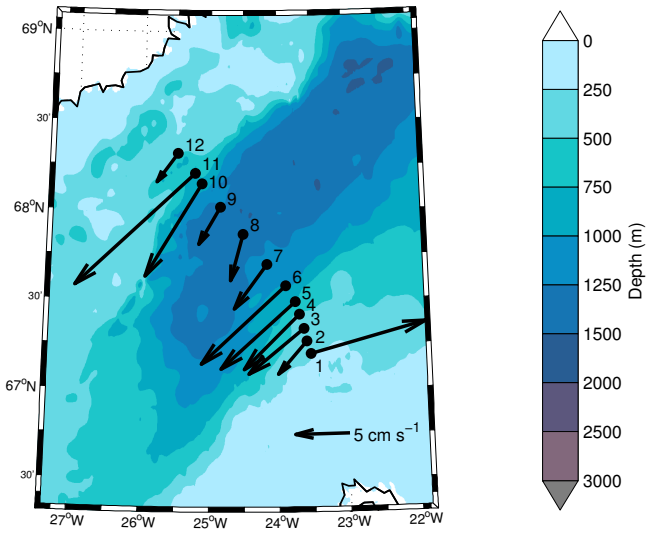

Figure 3: Study region in the Denmark Strait. The locations of the 12 moorings of the Kögur array are shown by black circles and are labeled 1–12 from the southeastern mooring. Vectors are the record-long mean velocities over the upper 500 m measured by each mooring. The bathymetry is from ETOPO5.

Point hydrographic measurements. A combination of Sea-Bird MicroCATs and SeaCATs were used (hereafter referred to as MCs), some with pressure sensors and some without. The sampling interval was either one hour or 15 minutes, and the temperature and salinity data were calibrated using several methods. The instruments that were not turned around in the field for a second year (a subset of the

moorings were redeployed) underwent post-deployment calibration at Sea-Bird. For the instruments that were redeployed, in-situ calibration casts were conducted using the shipboard conductivity-temperature-depth (CTD) package. The MC data were also compared to historical CTD data in the vicinity of Denmark Strait and to instruments on neighboring moorings to determine any drifts or offsets. Many MCs required no post-deployment adjustments (none for temperature), but 15 were corrected for small linear drifts or constant offsets in salinity.

Profiling hydrographic measurements. At sites KGA1–KGA5 coastal moored profilers (CMPs) were used to obtain vertical traces of temperature and salinity at 8 hour intervals which were averaged in 2 dbar bins. The data were calibrated through comparison with the fixed MCs located just below the bottom of the profiling range of each CMP. Most of the comparisons showed good agreement, but at KGA1 and KGA4 the salinity varied non-linearly for certain periods during the deployment. The record at KGA4 was corrected by matching the bottom CMP value to the salinity of the fixed MicroCAT at that depth. However, the ill-behaved record at KGA1 could not be corrected beyond November, and hence was truncated at that point.

Point velocity measurements. Aanderaa RCM and Nortek AquaDopp current meters were used throughout much of the array, sampling at either 15 minute or 1 hour intervals. The compasses were calibrated before deployment and the data were quality controlled for spikes and other non-physical variation.

Profiling velocity measurements. Three types of Acoustic Doppler Current Profilers (ADCPs) were used: 75 KHz RDI Longrangers, 300 KHz RDI Workhorses, and one 600 kHz Aanderaa Recording Doppler Current Profiler (RDCP). In each case a profile was obtained every hour (except for the RDCP that recorded a profile every 2 hours). The ADCP compasses were calibrated pre- and post-deployment,

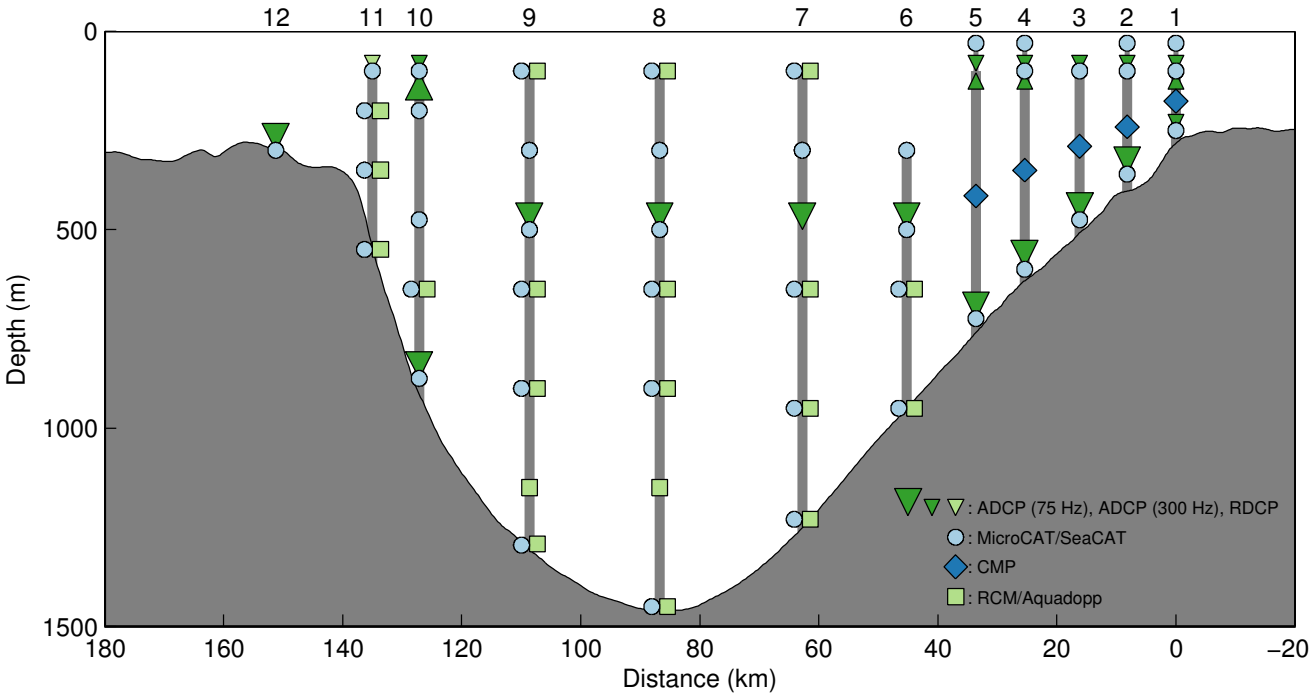

Figure 4: Diagram of the instruments recovered and their locations across the Kögur Array. The instruments are, ADCP: Teledyne RDI Acoustic Doppler Current Profiler (LongRanger (75 Hz) and WorkHorse (300 Hz)), RDCP: Aanderaa Recording Doppler Current Profiler, MicroCAT/SeaCAT: Sea-Bird 37 MicroCAT or 16plus SeaCAT C-T (P) Recorder, CMP: Coastal Moored Profiler (profiling CTD), RCM: Aanderaa Recording Current Meter, Aquadopp: Nortek Acoustic Doppler Current Meter. The two Instruments lost were a MicroCAT at 100 m on KGA 6 and a MicroCAT at 50 m on KGA 3. Bathymetry is from an underway inverted echosounder (Våge et al., 2013).

and the accuracy of the data was also assessed by comparing various point current meter measurements with overlapping ADCP bins on the same mooring. In all cases the speeds recorded were in good accordance with each other. However, for some of the ADCPs the current direction showed an offset that depended on the compass heading measured by the instrument. Harden et al. (2014a) documented this type of behavior in a different moored application and attributed it to an asymmetric distribution of metal around the compass of the ADCP (see also von Appen (2014)). Following their method, we corrected for this by fitting a sinusoidal function, $y = Asinx + Bsin2x$, where A and B are constants

determined by least squares fits, to the angle discrepancy measured at overlapping bins (y) as a function of the ADCP heading (x) (National Geospatial-Intelligence Agency, 2004). This angle correction could then be applied to the ADCP velocities at all depths as a function of ADCP heading. This method was only applied to the ADCPs that showed a significant sinusoidal direction offset as a function of their heading.

The overall data return for the array was excellent: only two deployed instruments were lost (MCs at 100 m on KGA6 and at 50 m on KGA3) and, of those that were recovered, the vast majority returned a full 11 months of data. The only notable exceptions were the ADCPs at 100 m and 875 m on KGA10 which lasted until May, and the CMPs on KGA1, KGA3 and KGA5 which stopped profiling in May, October, and May, respectively. In addition, the MC at 300 m on KGA6 lost its buoyancy in October and fell to $\sim$700 m for the remainder of the deployment period. A detailed description of all the instrumentation and processing can be found on the Kögur Array website (http://kogur.whoi.edu).

Following previous studies (e.g. Nikolopoulos et al., 2009), we constructed vertical sections of velocity and hydrography using a Laplacian-spline interpolator, with a temporal resolution of 8 hours and spatial resolution of 8 km in the horizontal and 50 m in the vertical. For the hydrographic sections, a hybrid scheme was used where the interpolation was done in depth space in the upper part of water column, and in density space in deep water (using a technique for merging the two, see AppendixA). We found that this resulted in a more physically sensible state of the deep water column structure than the conventional depth gridding (see AppendixA for full details).

Transport estimates for the overflow water were calculated from the gridded density and velocity fields. Following previous studies, we use a potential density of 27.8 $\mathrm{kg\,m^{-3}}$ as the upper limit of DSOW (Dickson et al., 2008). We note that earlier estimates of DSOW transport in the Denmark Strait

were confined to the part of the water column above sill depth (∼650 m, see for example Våge et al. (2013)). However, since our array extends across the full depth of the Blosseville Basin there is no need for us to invoke this constraint; indeed we are able to determine if there is any aspiration as the overflow water approaches the sill (see Section 4.1). AppendixB outlines the method used to estimate the errors in the transport estimates.

When presenting the year-long average hydrographic sections across the array, we opt to show median sections rather than mean sections. This is because the nature of the hydrographic structure on the Greenland side of the strait results in an unphysical time mean. In particular, there is a sharp bend in potential temperature - salinity (Θ-S) space associated with the warm and salty EGC water near 300 m depth (see Figures 5 and 6), and space-time variations in this feature, together with the discrete sampling of the array, lead to mean values that greatly reduce (or remove) the subsurface salinity and temperature maxima. As such, the mean Θ-S properties on the western side of the strait are never realized in individual sections. The median section, however, produces both physical Θ-S properties and maintains the subsurface temperature and salinity maxima of the EGC water. The average velocity (in both the year-long mean and shorter time period means) has no such issues.

Ancillary data were used for parts of the study. To help shed light on the the upstream sources of the overflow waters we use the historical hydrographic dataset from the Iceland Sea region used by Våge et al. (2013). This product spans the period 1980 – 2012 and combines profiles from various institutional and public databases. For assessing the wind field in the Denmark Strait we use the ERA-Interim global reanalysis product from the European Center for Medium-Range Weather Forecast (ECMWF), which covers the period 1979 to present (Dee et al., 2011). This is a weather prediction model with an effective horizontal resolution of 80 km, which assimilates meteorological data to produce a "best-approximation"

of the atmosphere every 6 hours. It is accurate in the region of interest (Harden et al., 2011) and has been used in other studies of air-sea interaction along the coast of Greenland (Harden et al., 2014a,b). For our study we use 6-hourly near-surface fields (10-m wind, mean sea level pressure) for the period of the mooring array, and monthly means of the same fields for the period 1979 – 2012.

3. Year-long Average Hydrographic and Velocity Structure in northern Denmark Strait

The year-long mean along-stream (cross-transect) velocity measured by the array is predominantly equatorward and consists of two main flow features (Figures 3 and 5). On the Greenland side, the surface-intensified East Greenland Current is situated at the shelfbreak with a maximum velocity of 30 cm s^{-1}. On the Iceland side, a region of enhanced equatorward flow of order 10 cm s^{-1} is centered near the 1000 m isobath, spanning moorings KGA2–8. However, Våge et al. (2013), in their four synoptic shipboard occupations of the Kögur line, described not one but two distinct current features on the Iceland slope. The first was the NIJ, a mid-depth intensified flow located near the 650 m isobath. The second was the separated EGC, a surface intensified current located seaward of the NIJ that they argued bifurcated from the Shelfbreak EGC upstream of the section. Our mooring data indicate that, in the mean, the NIJ and separated EGC are not distinct but appear as a single feature at this location. However, the distinguishing characteristics of the two currents are evident in the mean velocity section. In particular, on the seaward side of the feature the flow is surface intensified, while on the shoreward side it is mid-depth intensified associated with diverging isopycnals progressing offshore. Indeed, in individual sections there is evidence of two distinct currents at times, while at other times one or both of the features are absent. Since the NIJ is observed as a single distinct current upstream of the Kögur line (Våge et al., 2011b; Jónsson and Valdimarsson, 2012) it is reasonable to assume that if the mooring array had been situated farther to the north the two currents would appear as separate features.

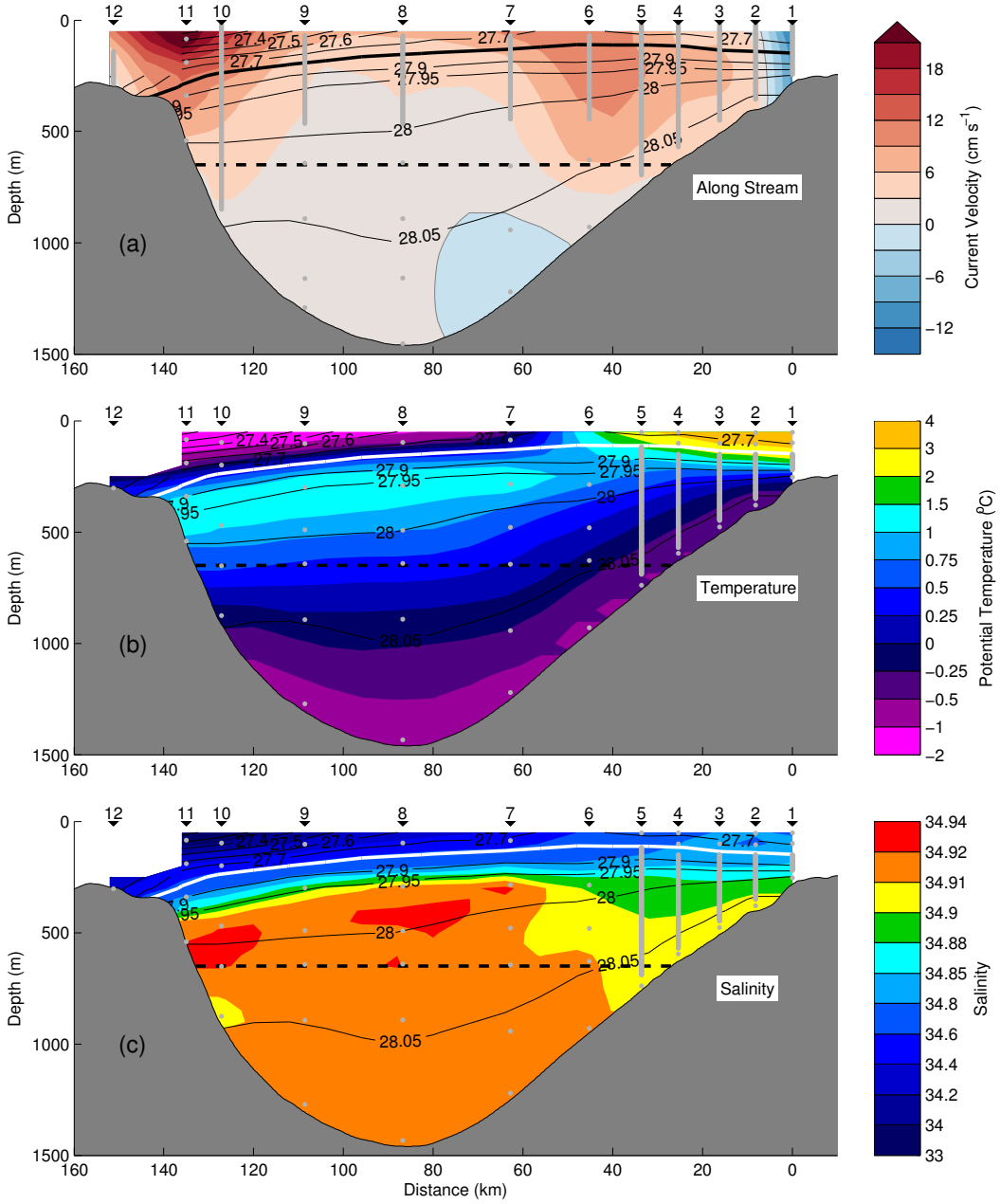

Figure 5: Year-long averages of gridded properties. (a) Mean along-stream velocity (cm s^{-1}); (b) median potential temperature (°C); and (c) median salinity. The mooring numbers are listed above each panel. Overlaid on all panels is the median potential density (kg m^{-3}) with the 27.8 kg m^{-3} isopycnal highlighted in bold. The bathymetry is from an underway echosounder (Våge et al., 2013). Typical raw data locations (i.e. not during mooring blow-down events) are shown by gray dots. The Denmark Strait sill depth is indicated by the dashed line.

In addition to these two equatorward flows, there are two regions of mean poleward velocity. One is at the southern end of the array (captured by KGA 1) and is the seaward edge of the NIIC, which advects warm subtropical-origin water into the Nordic Seas (Figure 1). The other is a relatively weak (< 5 cm s^{-1}) flow on the Iceland slope below sill depth, which we discuss further below (Section 5).

The median hydrographic sections reveal four primary water masses (Figure 6). At the surface, there is a wedge of cold, fresh Polar Water (Θ < 0°C, S < 34) situated on the northern end of the section; the resulting hydrographic front supports the surface intensified Shelfbreak EGC. This freshwater originates from the Arctic Ocean (e.g. de Steur et al., 2009), and, while most of it resides on the Greenland shelf, it extends significantly offshore of the shelfbreak at this location (see also Våge et al. (2013)). On the opposite end of the section, also in the upper layer, warm and salty subtropical-origin water (Θ > 2.5°C, S > 34.78) extends out to mooring KGA4. This water originates from south of Denmark Strait and is referred to as Irminger water. North of the strait it is partly fluxed seaward from the NIIC (Jónsson and Valdimarsson, 2012) and mixes with the ambient water on the slope, leaving a modified signature at the Iceland shelfbreak in our data.

The other two water masses are situated below the 27.8 kg m^{-3} isopycnal, which is the upper boundary of DSOW. The deepest water mass in the section is Arctic Origin Water (Θ < 0°C, σ_Θ > 28 kg m^{-3}) which occupies the deep basins of the Nordic Seas. At the Kögur line it is found below 800 m on the Greenland side, but is banked up on the Iceland slope to as shallow as 300 m. Above this, towards the Greenland side, is a subsurface core of warmer and more saline water (Θ > 0°C, S > 34.9, σ_Θ > 27.8 kg m^{-3}) known as Return Atlantic Water. Mauritzen (1996) demonstrated that this water mass stems mostly from the portion of the Norwegian Atlantic current that recirculates southward at Fram Strait (Figure 1); as the water flows around the perimeter of the Nordic Seas it cools through air-sea interac-

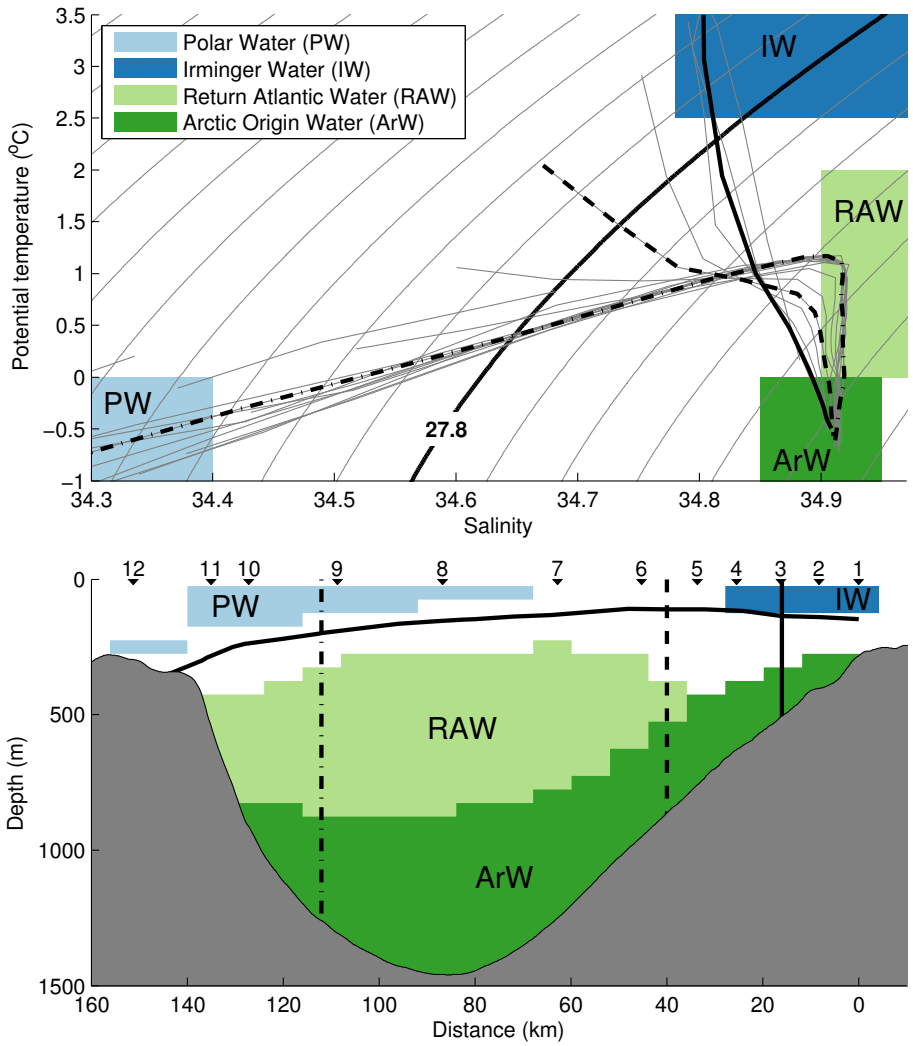

Figure 6: Water masses in the northern Denmark Strait. Top: Θ-S properties of all vertical profiles from the gridded median sections (gray lines). The four major water masses are distinguished by color (see the legend). Density contours are plotted every 0.05 kg m^{-3} and the solid black density surface is the 27.8 kg m^{-3} isopycnal. Three profiles have been highlighted with bold, dashed, and dot-dashed lines, near moorings KGA3, KGA6 and KGA9, respectively. Their locations are shown on the bottom panel. Bottom: Vertical section showing the location of the four water masses in the median section. The mooring numbers are listed above the panel. The median 27.8 kg m^{-3} isopycnal is contoured in black.

200 tion. There is also a contribution from the transformed Atlantic Water that has circulated throughout the
201 Arctic Ocean. Mauritzen (1996) argued that nearly all of the DSOW was comprised of Return Atlantic

Water, although with the discovery of the NIJ we now know that this is not true (Våge et al., 2011b). The Return Atlantic Water fills much of the middle water column in the median Kögur section, and extends some 40 km onto the Iceland side of the Blosseville Basin. However, note that inshore of mooring KGA5 on the Iceland slope, the section is devoid of this water mass.

Figure 6 shows the location of these four primary water masses in Θ-S space, as well as their geographical distribution across the mooring array. For context we have included the Θ-S profiles from each grid point across the median Kögur section, and have highlighted a profile on the Greenland side, one on the Iceland side, and one in between (within the equatorward current on the Iceland slope). All of the Θ-S profiles emanate from depth in the Arctic Origin Water (which extends across the entire section, though not at the same depth horizon). However, the highlighted profile on the Greenland side then passes through the Return Atlantic Water before bending sharply to fresher values, ending in the Polar Water (near the surface). By contrast, the highlighted profile on the Iceland side does not pass through either of these water masses, but ends up in the Irminger Water near the surface. This different hydrographic character is used below to quantify the separate water mass components of the DSOW (Section 5).

In the median hydrographic sections of Figure 5, we note that both the transition from Polar Water to Irminger Water in the upper layer, and from the Return Atlantic Water to Arctic Overflow Water at depth, align with the mean equatorward current on the Iceland slope. This corroborates our interpretation of this mean current as a composite of the separated EGC, advecting these two water masses, and the NIJ, which transports Arctic Origin Water at depth. This is consistent with the view presented by Våge et al. (2013).

Due to the lack of Return Atlantic Water on the Iceland slope inshore of KGA5, it is likely that the

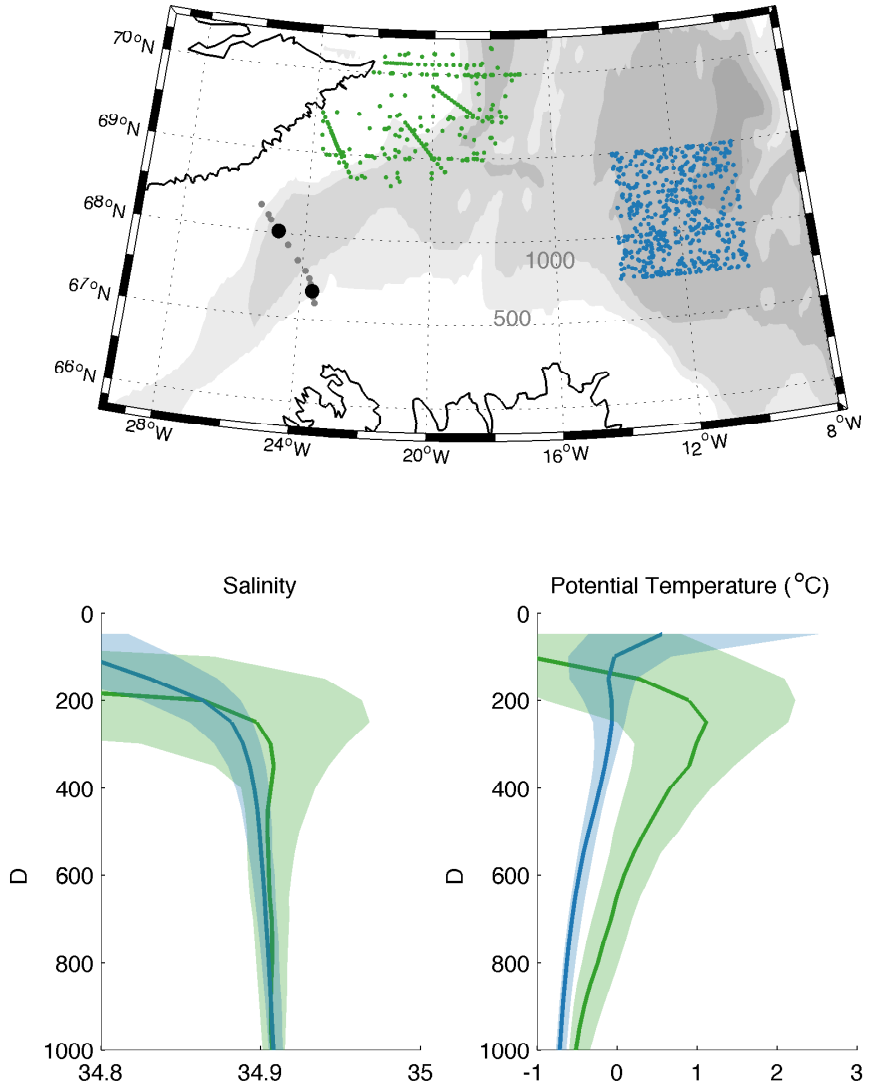

Figure 7: Top: Upstream location of hydrographic profiles from the historical database (1980–2012) divided into regions representative of the Greenland shelf/slope (green) and the central Iceland Sea (blue). The locations of the moorings in the Kögur Array are indicated by the gray dots. KGA3 and KGA9 are highlighted as the representative moorings used in Figure 8. The bathymetry is from ETOPO5 at 500 m increments. Bottom: Salinity (left) and potential temperature (right) from the regions shown in top panel (colors) as a function of depth. The solid lines are the 50 m depth-binned median of all profiles. The shaded regions span the 10th – 90th percentile of all depth-binned data.

overflow water here has a different origin than the water within the two branches of the EGC, as proposed by Våge et al. (2011b). They hypothesized that the NIJ water originates from the central Iceland Sea, as opposed to the Nordic Seas boundary current system. To investigate this further, we examined the historical hydrography in two regions: one in the central Iceland Sea, and the other along the Greenland shelf/slope upstream of the mooring array (Figure 7).

The vertical profiles in the Iceland Sea are clearly distinct from those along the Greenland shelf/slope. This can be seen by comparing the median temperature and salinity profiles from the two regions (Figure 7b). In the Iceland Sea there is no sub-surface maximum in either property, which is reminiscent of the Iceland side of the Kögur Array. Furthermore, the Θ-S properties in the Iceland Sea support the view that this is the source of the water within the NIJ, while the Θ-S properties upstream of the Kögur array along the Greenland shelf/slope are consistent with those on the western side of the array. This is demonstrated by constructing volumetric Θ-S plots of the two regions for the water shallower than 1000 m (Figure 8). The distribution of Θ-S for the Greenland shelf/slope agrees well with the deep portion of the median profile at mooring KGA9 (on the western side of the array), while the same is true for the Iceland Sea and mooring KGA 3 (on the eastern side).

Our evidence thus supports the hypothesis put forth by Våge et al. (2011b) that two sources feed the Denmark Strait Overflow, one containing Return Atlantic Water from the Nordic Seas boundary current, and the other containing water resident in the Iceland Sea. Our mooring data also support the view of Våge et al. (2013) that the Return Atlantic Water is advected towards the strait within two branches of the EGC: a shelfbreak branch, and a separated branch in the interior of the Blosseville Basin.

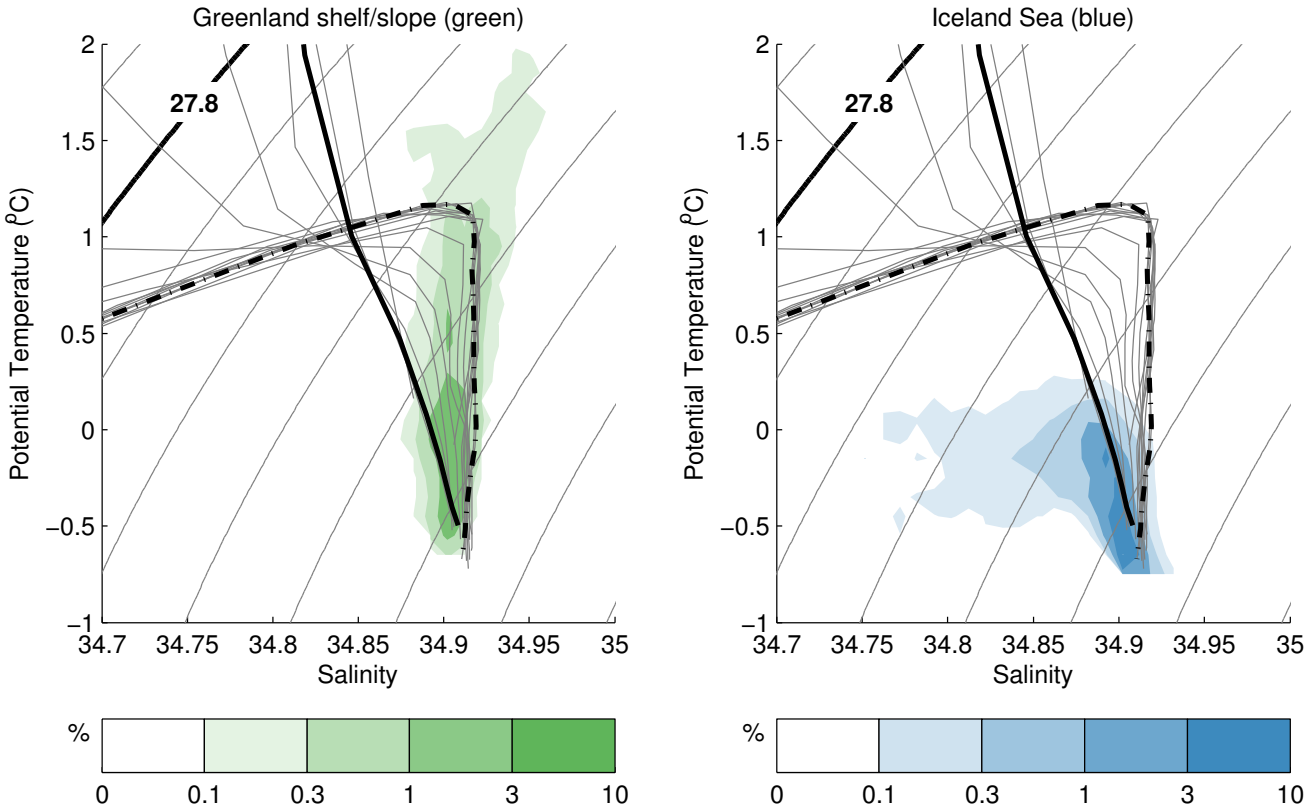

Figure 8: Volumetric Θ-S (colors) for hydrographic data shallower than 1000 m from the two geographic regions highlighted in Figure 7: the Greenland shelf/slope (left) and the Iceland Sea (right). For the calculation, the Θ-S properties were divided into temperature bins of width 0.1°C and salinity bins of width 0.01. Values are plotted on a log scale as a percentage of the total data. Overlaid are the median Θ-S profiles across the array from the gridded product (gray lines), with the nearest grid points to the two moorings KGA3 and KGA9 highlighted by the bold and dot-dashed lines, respectively (see Figure 6b). Density contours are plotted every 0.05 kg m^{-3} and the solid black density surface is the 27.8 kg m^{-3} isopycnal

4. Total Overflow Transport

As seen in Figure 5, the Kögur array captures the majority of the DSOW being transported into the Denmark Strait. Before presenting transport estimates, however, there are a few aspects of the flow that need to be discussed – in particular, aspiration, recirculation, and the surface outcropping of the 27.8 kg m^{-3} isopycnal.

4.1. Aspiration

Aspiration refers to the process whereby water below sill depth is drawn upwards and participates in an overflow. This is known to happen in the Mediterranean outflow (Kinder and Parrilla, 1987) as well as the Faroe Bank Channel Overflow (Hansen and Østerhus, 2007). Notably, Våge et al. (2011b) and Våge et al. (2013) were able to balance mass between the transport at the sill estimated by Jochumsen et al. (2012) and the upstream sources of DSOW by only considering equatorward flow above sill depth. As such, they assumed that aspiration did not occur in Denmark Strait (within the error bars of their measurements). However, these studies used only a small number of synoptic shipboard sections upstream of the strait, and Jochumsen et al. (2012)'s estimate at the sill is based on only two moorings constrained by a numerical model. Consequently, there is inherent uncertainty in such a mass balance. The extensive cross-strait and vertical coverage of the Kögur array provides us with an opportunity to look for evidence of aspiration over a year-long period.

The mean equatorward transport at the Kögur array below sill depth (650 m) for 2011–12 is 0.58 $\pm$ 0.07 Sv (Figure 9). With no exit downstream, this water has no option but to ascend towards the sill and contribute to the overflow. The deep transport varies on synoptic timescales (as does the total transport), but it seems apparent that, in the mean, there is significant aspiration in Denmark Strait that previous studies were unable to detect. In our transport estimates below, we therefore integrate vertically all the way to the bottom of the array.

4.2. Recirculation

On the Iceland side of the median section, the 27.8 kg m^{-3} isopycnal does not intersect the bottom (Figure 5). In fact, in only 2% of the individual sections does this happen, and in roughly 50% of sections the isopycnal is shallower than 150 m on the southern end of the array. Notably, the flow at this end of

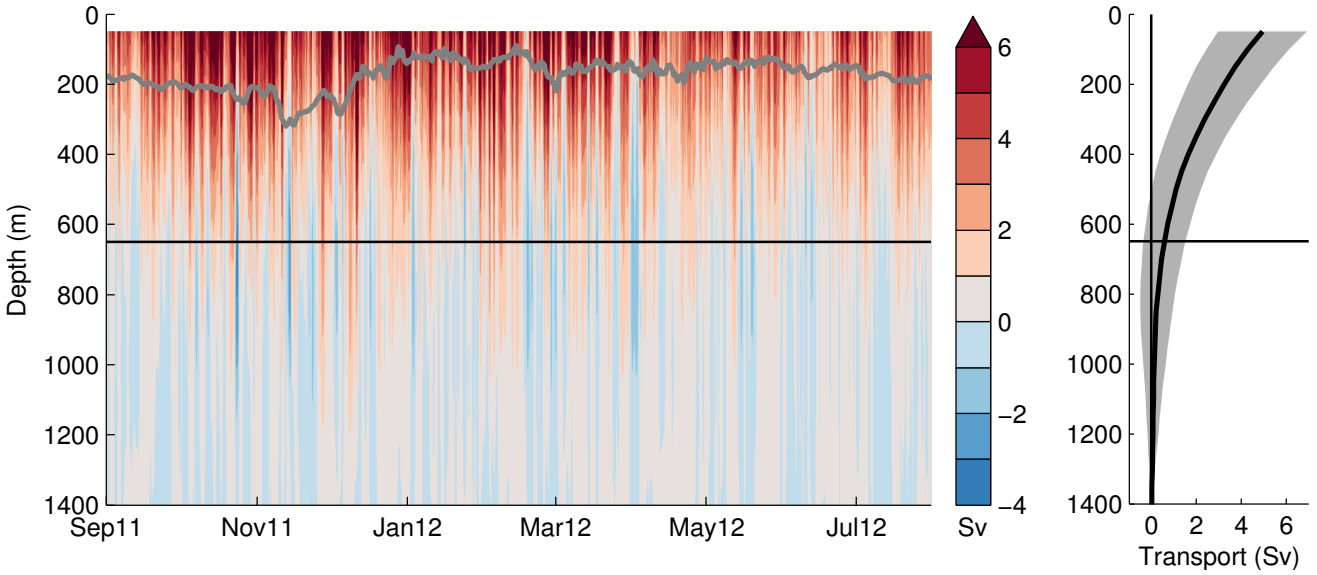

Figure 9: Left: Cumulative net transport across the array from the bottom of the section to the top as a function of time. The black line indicates the depth of the sill (∼650 m). The gray line is the mean depth of the 27.8 kg m^{-3} isopycnal across the array. Right: Mean cumulative transport over the record length with the sill depth indicated. The shadows denote the uncertainty.

the array is predominantly poleward; only 10% of sections contain equatorward flow below the 27.8 kg m^{-3} isopycnal. Therefore, not only does the array miss some of the overflow transport on the Iceland side of the array, but (in the mean) the part that is missing is flowing poleward. South of the sill, the 27.8 kg m^{-3} isopycnal is deeper than 1000 m (Våge et al., 2011a) and so this can not be the source of the northward flowing dense water. It therefore has to be recirculation of water that previously passed through the array but did not progress over the sill into the Irminger Sea. It seems likely that this dense water joins the northward-flowing NIIC on the outer portion of Iceland shelf (Figure 1).

Fortunately, over the last decade there have been seven synoptic shipboard occupations of the Kögur section that include velocity measurements and extend onshore of the Iceland shelfbreak, hence completely capturing the overflow water. This permits us to make a rudimentary estimate of the missing

281 northward transport. In all seven sections, the flow is poleward onshore of the shelfbreak with a mean
282 transport of -0.15 $\pm$ 0.05 Sv. We found no clear relationship between the individual transports and either
283 the 27.8 kg m^{-3} isopycnal height or the velocity at the shelfbreak. As such, we have no way of assessing
284 this missing transport in our array on a section-by-section basis. We do, however, subtract the mean
285 shipboard value from our transport estimates for both the total transport and that of the NIJ.

286 *4.3. Surface Outcropping*

287 Over the course of the winter, surface cooling reduces the stratification of the upper water column
288 and the 27.8 kg m^{-3} isopycnal rises towards the surface (Figure 9). Consequently, in 32% of the sections,
289 the 27.8 kg m^{-3} isopycnal "outcrops" above our upper bound of gridding (50 m) and hence results in a
290 missing contribution to our transport estimates. We accounted for this by assuming that the velocity in
291 the upper layer is equal to that at 50 m and that the 27.8 kg m^{-3} isopycnal also outcrops at the surface
292 in these instances. We note that these assumptions are counteracting to some degree; it is likely that the
293 velocity will actually increase towards the surface, while the 27.8 kg m^{-3} is unlikely to outcrop at the
294 surface in all cases. For times when the 27.8 kg m^{-3} isopycnal outcrops at the top of the gridded section,
295 the estimated mean missed transport is 0.10 $\pm$ 0.01 Sv. In what follows, we apply this missed transport
296 on a section-by-section basis.

297 *4.4. Total Transport*

298 We now estimate the total transport of the DSOW through the Kögur array, subject to the adjustments
299 described above (Figure 10a). Over the full deployment period, the mean transport of overflow water is
300 3.54 $\pm$ 0.16 Sv (uncertainty quoted is a standard error – see AppendixB for full treatment of errors). This
301 is the first time that the complete transport of overflow water through Denmark Strait has been robustly

estimated and compares well to previous long-term term estimates made at the sill of 3.4 Sv (Macrander et al., 2005; Jochumsen et al., 2012) and to the 3.6 Sv from a recent modeling study (Sandø et al., 2012).

The transport is largely stable throughout the year, although there is evidence of a weak seasonal signal; a sinusoidal fit with amplitude 0.63 Sv explains 7% of the variance at the annual period (Figure 10a) . This seasonal signal peaks in fall and winter and is weakest during spring and summer. This is in accordance with the weak seasonal signal observed by Jochumsen et al. (2012) at the sill. However, like their study, the seasonal signal at the Kögur line is weak in comparison with both the year-long mean and the shorter timescale synoptic variability. It should also be noted that, although a sinusoid fits the data, it does not necessarily imply that this variability is seasonally driven and may just represent longer period variations in the total transport as observed by Jochumsen et al. (2012) at the sill.

The total transport time series shows significant synoptic variability, with strong signals at periods of 2 – 4 days (evident in the wavelet spectra, not shown). This synoptic variability exists throughout the section, including below sill depth. Similar high frequency fluctuations in transport are common at the sill (Jochumsen et al., 2012) which affect the downstream evolution of the overflow plume (von Appen et al., 2014). Our results indicate that this variability is present in the flow of dense water approaching the sill. At this point the nature and cause of this variability is unknown, as is its link (if any) to the fluctuations in overflow transport at the sill. This will be the subject of a future study.

5. Partitioned Transports

In Section 3 above we established the likelihood of two distinct geographical sources of the overflow water: one associated with the Nordic Seas Boundary current (the EGC system), and the other from the Iceland Sea via the NIJ. In this section we aim to partition the overflow waters between these two sources to assess their relative importance and shed light on what drives their variability in transport. Despite

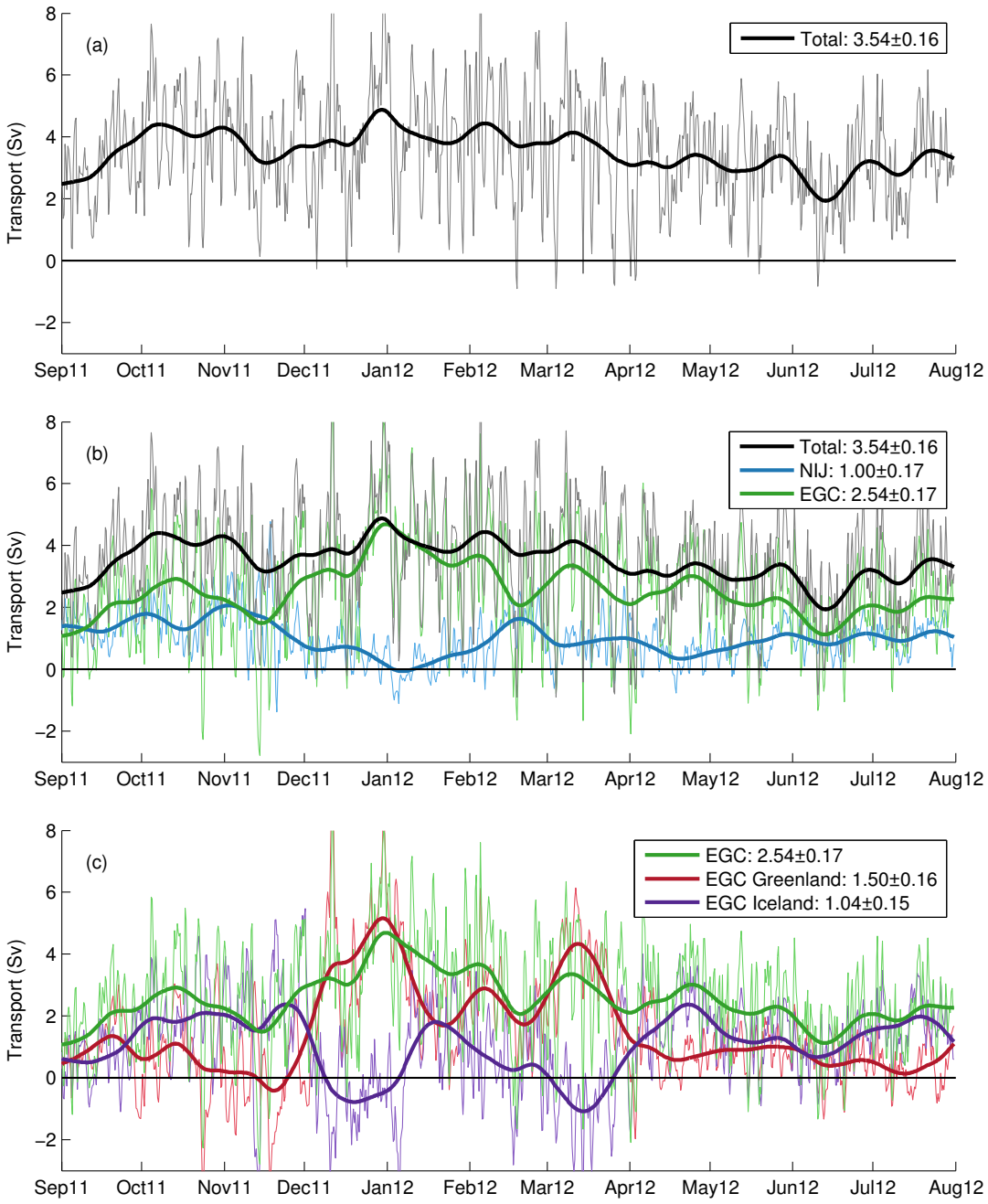

Figure 10: Time series of the transport of overflow water (denser than 27.8 kg m^{-3}) through the Kögur Array. Light colors are the synoptic estimates and dark colors are the 30-day smoothed values. The panels are: (a) Total transport; (b) Transport partitioned between North Icelandic Jet (NIJ) and East Greenland Current (EGC); and (c) EGC transport partitioned between the Greenland and Iceland continental slopes.

the evidence that the separated EGC and NIJ are distinct currents (particularly upstream of the array), it is problematic to distinguish them at the Kögur line based solely on their velocity signatures. This is because both features are dynamic, intermittent, and often merged (as in the mean). Consequently, we developed a procedure to distinguish the transport within each component using the hydrographic data.

5.1. Partitioning Method

Both the Shelfbreak and separated EGC have distinct sub-surface salinity maxima, in contrast to the NIJ which has no such feature (Figures 5 and 6). We thus use this difference in hydrographic structure to distinguish and divide the transport contributions from the two sources. Our method is as follows. We identified two moorings that act as water mass end members in the array: KGA2 for the Arctic origin water within the NIJ, and KGA7 for the Return Atlantic water within the EGC. (In this calculation we do not distinguish between the Shelfbreak and separated EGC, but consider the composite transport of both branches.) These two moorings always display the typical Θ-S properties of the two respective water masses, and the boundary separating them always lies between the two moorings. Furthermore, all profiles between these end members can be constructed by a linear superposition of the two end members. We can therefore use these end members to assess individual vertical profiles at the grid points between KGA2 and KGA7 in each synoptic section to determine which end member the profile in question most resembles.

Specifically, we compare individual salinity profiles in density space to the salinity of the end members within the overflow layer, with a grid spacing of 0.01 $\mathrm{kg\,m^{-3}}$. We apply a running median filter to the records of the two end members at each of these density levels with a width of 14 days, allowing the end member properties to evolve throughout the year. The relative contribution from the two end members is then quantified using the following metrics:

$$
\begin{aligned}
n_{NIJ} &= \left(\sum_{\rho=27.97}^{28.03} \left[S_{NIJ}(\rho) - S_i(\rho) \right]^2 \right)^{\frac{1}{2}} \\
n_{EGC} &= \left(\sum_{\rho=27.97}^{28.03} \left[S_{EGC}(\rho) - S_i(\rho) \right]^2 \right)^{\frac{1}{2}} \\
\%_{EGC} &= 100 \cdot \frac{n_{NIJ}}{(n_{NIJ} + n_{EGC})} \\
\%_{NIJ} &= 100 \cdot \frac{n_{EGC}}{(n_{NIJ} + n_{EGC})},
\end{aligned}
$$

where $S_{NIJ}(\rho)$ and $S_{EGC}(\rho)$ are the running median salinity end members as a function of density for the NIJ and EGC, respectively, and $S_i(\rho)$ is the salinity of the profile in question as a function of density. We chose the upper and lower density bounds for the sum based on the portion of Θ-S space where the end-member profiles are diverging (Figure 6). The quantities n_{NIJ} and n_{EGC} are therefore the RMS error between the salinity of the profile and each end member, and $\%_{NIJ}$ and $\%_{EGC}$ represent the effective percentage of water from each end member in the profile. By definition, $\%_{NIJ} + \%_{EGC} = 100$.

Applying this procedure for the profiles of an individual synoptic section, we can thus divide the section into waters from each source. We chose 60% as the threshold for a profile to be representative of an end member. The 40% – 60% region is therefore a "soft" boundary between the two sources and allows for some degree of mixing to have taken place. We assign 50% of the transport in this transition region to each source water. An example of this routine as applied to one section is shown in Figure 11.

Space-time Hovmöller plots demonstrate the results of our source water partitioning routine (Figure 12). One sees that the calculated water mass boundary tracks the salinity front between the Return Atlantic Water and Arctic Origin Water (top panel), and also tracks the enhanced transport associated with the separated EGC / NIJ (middle panel). The boundary varies on similar timescales as the velocity field, i.e. from synoptic to seasonal. For example, it is generally closer to the Iceland shelfbreak during

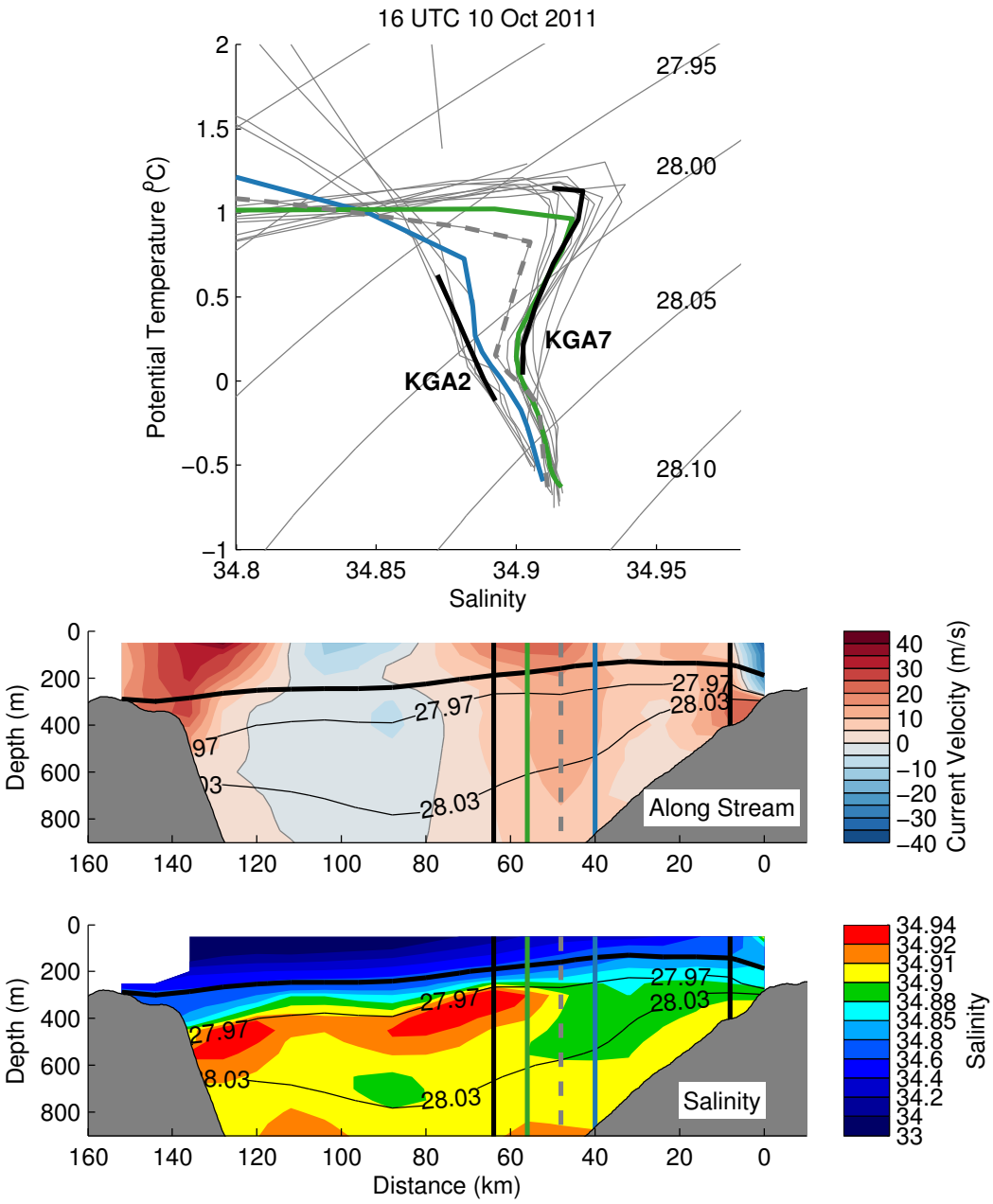

Figure 11: Example of the partitioning routine as applied to the section at 16 UTC on October 10, 2011. Top: Θ-S properties for all gridded profiles across the section (gray lines), the 14-day running median end members over the density range used for comparison (thick black lines), the last profiles deemed to be solely in the East Greenland Current or North Icelandic Jet waters (green and blue lines, respectively), and profiles that fall in the "soft boundary" region between end members (dashed thick gray line; in this case there was only one such profile). Bottom: The corresponding along-stream velocity and salinity sections. The colors of the profiles are the same as in the top panel. Note that the end member profiles (black lines) extend over the whole depth and not just the density range as in the upper panel. The density range used for the comparison is highlighted by the two thin contours, and the 27.8 kg m^{-3} is bold.

the winter and spring months (Figure 12). It should be noted that instrument dropouts affect the accuracy of our method. The MicroCAT at 300 m on KGA6 was lost in November and the Moored Profiler on KGA5 stopped sampling in May. Both of these regions are important for defining the boundary between source waters and, as such, the boundary becomes less well defined as the year progresses (Figure 12). This is particularly evident after May when the calculated boundary region essentially becomes static. However, as is shown below, this restriction is not critical for determining the seasonal movement of the water mass boundary and its relationship to the flow field.

5.2. Partitioned Transports

Over the year-long period of the array, the equatorward transport of overflow water in the East Greenland Current system (i.e. the combination of the Shelfbreak EGC and Separated EGC) was more than twice that of the NIJ: 2.54 $\pm$ 0.17 Sv versus 1.00 $\pm$ 0.17 Sv (Figure 10b). However, this division varies significantly over the course of the year on a variety of time scales. Furthermore, to some degree the two sources compensate each other. Recall that for the total transport there was relatively little variation over the year (although there was some indication of enhanced equatorward flux in the winter). One sees in Figure 10b, however, that the fluctuations in the two components are much larger. For example, more East Greenland Current water flows through the Strait in the winter and spring months, which coincides with a general reduction in the NIJ transport. Both of these seasonal signals are proportionally slightly stronger than for the total transport (amplitudes of 0.82 Sv and 0.40 Sv, respectively), although they still only account for 11% and 13% of the variance, respectively.

By definition, the transport of each component is dependent on both the cross-sectional area of the feature and also the mean velocity through that area. We find that on synoptic time scales the magnitude of the flow, rather than the area, drives the variation in transport. However, over longer periods, the

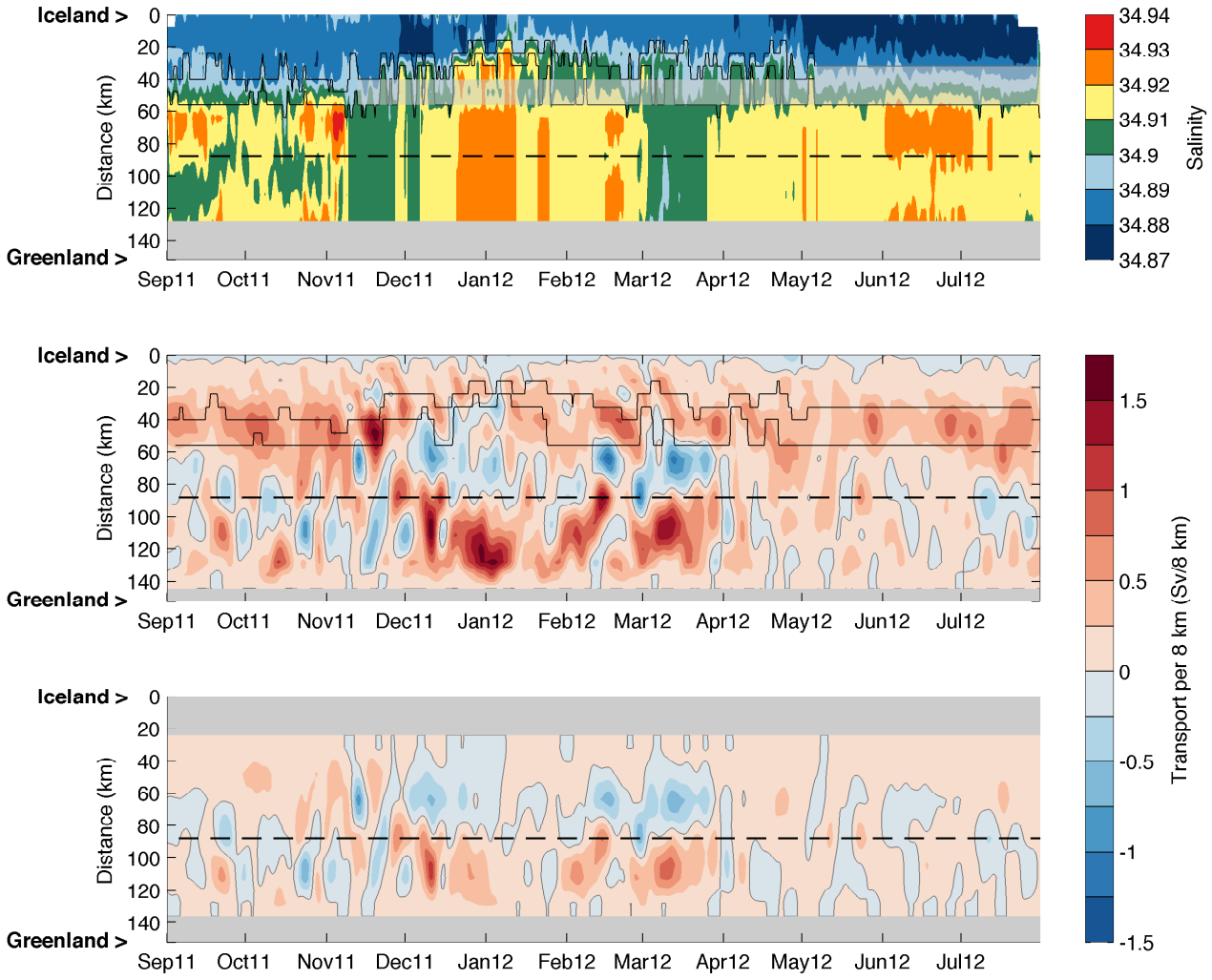

Figure 12: Top: Hovmöller plot of salinity on the 28 kg m^{-3} isopycnal. The x-axis is time, and the y-axis is distance along the array. Black contours denote the outer limits of boundary region from the detection routine. The gray transparent shading represents the portions of the record where key instrument dropout produces uncertainty in the location of the boundary, i.e. in this region we have lost data and hence have to interpolate properties across the range highlighted. Middle: Hovmöller plot of binned transport (in 8km-wide bins) below 27.8 kg m^{-3}, low-passed at 7 days. The black contours are the same as in the top panel except low-passed using a running median filter of 7 days. Bottom: Same as middle panel except for transport below sill depth ($\sim$650 m). The horizontal black dashed line in each panel marks the middle of the array.

area of each pathway significantly influences the transport variability. Not surprisingly, this is also associated with the lateral position of the boundary between the two water mass sources. For example, the beginning of January, beginning of March, and mid-April are all times of larger transport of EGC water, lower transport of the NIJ, and an excursion of the water mass boundary towards the Iceland shelfbreak (Figures 10b and 12). Therefore, much of the trade-off between the pathways is associated with lateral motion of the front between the two water masses as well as changes in the velocity field. It will thus be important to determine what controls the lateral extent of East Greenland Current water across the Blosseville Basin if we are to understand the partitioning of overflow source water in the Denmark Strait.

5.3. Shelfbreak vs Separated East Greenland Current

In the four synoptic shipboard occupations of the Kögur line presented by Våge et al. (2013), it was straightforward to identify the separated EGC as a surface intensified flow on the Iceland slope. Unfortunately, as discussed previously it is not always possible to define a clear separated EGC in our array data. It is of interest, however, to determine the partitioning of transport between this branch of the EGC and the shelfbreak branch. Taking the simplest approach possible, we divided the East Greenland Current transport between that which passes on the Greenland side of the array, and that which flows on the Iceland side. The former is taken to be the Shelfbreak EGC, and the latter the separated EGC. The center of the array is near mooring KGA8 (Figure 4), and at the grid point closest to that mooring we assigned half of the transport to each component.

The partitioning in transport between the two EGC branches is shown in Figure 10c. In the mean, slightly more overflow water is advected by the shelfbreak branch (1.50 ± 0.16 Sv) versus the separated branch (1.04 ± 0.15 Sv). What is striking about these time series, however, is that there is pronounced

406 variability throughout the year in each branch and they are clearly out of phase with each other – the
407 transports are significantly anti-correlated for periods of two weeks and longer (seen from coherence
408 spectra, not shown). Hence, when the flow is stronger on the Greenland side it is weaker on the Iceland
409 side, and vice versa. What could be partitioning the flow like this? Våge et al. (2013) contended that
410 the separated EGC forms as the result of eddies that detach from the shelfbreak branch upstream of the
411 Kögur array and migrate offshore, eventually coalescing into a semi-permanent jet on the Iceland Slope.
412 However, they also hypothesized that a portion of the separated EGC may be part of a wind-driven anti-
413 cyclonic gyre in the Blosseville Basin (with the northward return flow between the two EGC branches).
414 In our data, we see evidence of EGC eddies as well as gyre-like flow, and the latter seems to impact the
415 partitioning of the transport between the two branches over longer than synoptic time periods.

416 The synoptic sections from the array are highly variable with rotational, eddy-like features often
417 discernible in the upper water column. A detailed description of these features is beyond the scope of
418 this study and will be addressed in the future. Here we focus on evidence for longer timescale, gyre-
419 like circulation in the Blosseville Basin and how this manifests itself in terms of the EGC branches. In
420 general, over periods of weeks to months, whenever there is strong flow on the Greenland slope, there is
421 weaker flow on the Iceland slope. In some instances the flow on the Iceland side is in fact reversed (i.e.
422 northward, see Figure 10c), which is reminiscent of a cyclonic circulation in the basin. The opposite is
423 true as well, but to a lesser degree. An effective way to view this is to consider the flow below sill depth
424 away from the near-surface variability (see Figure 12, bottom panel). Cyclonic circulation is evident in
425 December, February and March, while weaker and less distinct anticyclonic circulation occurs at other
426 times, namely in October, November and July. The predominance of the cyclonic regime is reflected in
427 the mean velocity section below sill depth (note the deep flow reversal on Iceland slope in Figure 5).

Notably, this longer timescale partitioning of the East Greenland Current doesn't necessarily modify the flow of the NIJ. The transport of the NIJ seems to be more closely tied to the lateral position of the hydrographic front between the two sources (compare Figures 10b and 12a) and is not related simply to the transport of the separated EGC. The lateral motion of the front is, in turn, likely tied to the dynamics of the Separated EGC and NIJ. Nonetheless, our data suggest that the occurrence of gyre-like circulation in the Blosseville Basin affects the composition of the dense water that overflows the sill, and hence it is of interest to understand the cause of this variability.

5.4. Wind Forcing

We now address the role of wind forcing in driving the gyre-like circulation in the northern part of Denmark Strait. The mean atmospheric conditions for the year-long deployment period (Figure 13b) are similar to longer period means in the region (Harden et al., 2011). In particular, the Icelandic Low is situated over the Irminger Sea and this drives topographically enhanced barrier winds along the southeast coast of Greenland. The Denmark Strait therefore typically experiences winds from the northeast with stronger values on the western side of the strait. However, due to the upstream bend in the coastline at Scoresby Sund near 71°N (Figure 1), the curved flow through the region (from northerly to northeasterly) often produces a negative wind stress curl over the Blosseville Basin which Våge et al. (2013) argued might lead to an anticyclonic gyre north of Denmark Strait.

We contend as well that the gradient in the local wind across the northern part of Denmark Strait can lead to gyre-like flow in the Blosseville Basin, and argue that such a circulation pattern is time dependent and can switch from anti-cyclonic to cyclonic. To address this, we computed the mean gradient of the along-strait 10-m wind velocity (resolved onto an angle 45° from north and low-passed over two weeks) over the width of the array for the time period of the deployment using the ERA-Interim data set. This

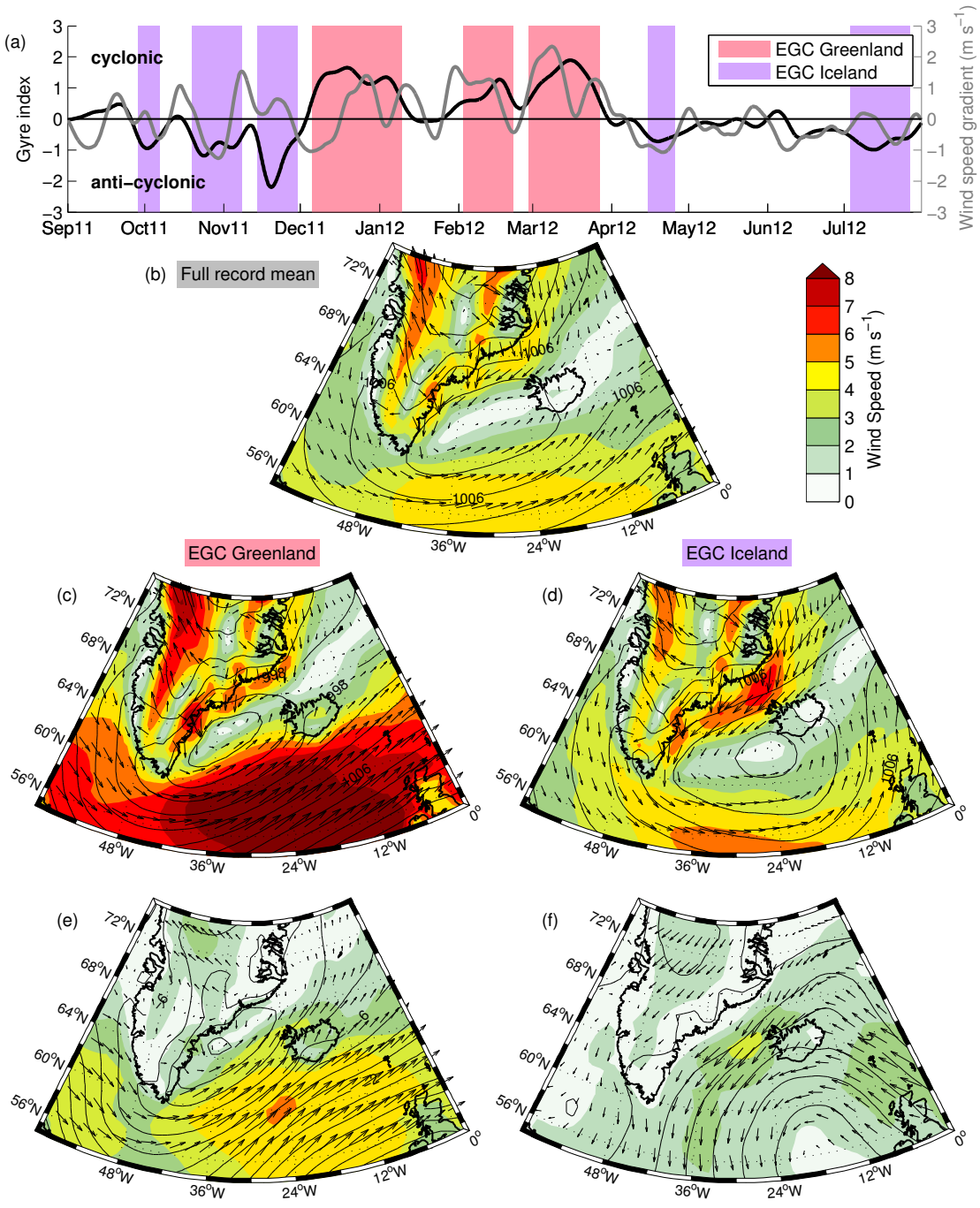

Figure 13: (a) Time series of the Gyre index (black) and cross-Strait wind gradient over the width of the array (gray) (see text for an explanation of the Gyre index). The shaded regions denote the times when the transports of each branch of the EGC are dominant. (b) Full record-long mean 10-m wind field (colors and vectors) and mean sea level pressure (black contours) from ERA-Interim over the length of the mooring deployment. (c-d) Composite vector wind and pressure fields from periods where flow on the Greenland and Iceland sides are dominant, respectively (see shaded regions in (a)). (e-f): Same as (c-d) but showing the anomalies from the mean wind and pressure field shown in (b).

can be thought of as the cross-strait torque with positive (negative) values meaning stronger (weaker) along-strait winds on the Greenland side versus the Iceland side (Figure 13a, gray line).

To investigate the impact of this wind gradient on the ocean, we produced an oceanic gyre index (G_i),

$$G_i = \frac{T_{EGCg} - T_{EGCi}}{T_{EGCg} + T_{EGCi}},$$

where T_{EGCg} and T_{EGCi} are the 14 day low-passed transports of the East Grenland Current through the Greenland and Iceland sides of the array, respectively. The gyre index is therefore positive (cyclonic) when the transport of the Shelfbreak EGC is larger than that of the separated EGC, and negative (anti-cyclonic) when the opposite is true (Figure 13a, black line).

The gyre index and wind speed gradient time series are weakly correlated with r = 0.42, which is significant at the 95% confidence level (dof = 30). The implication is that during periods of stronger winds over the Greenland slope, cyclonic circulation ensues which results in a larger proportion of the Return Atlantic Water flowing through the shelfbreak branch of the EGC versus the separated branch. The opposite is true for periods of stronger winds over the Iceland slope, which is associated with anticyclonic circulation in the Blosseville Basin.

To highlight these regimes explicitly, we composited the atmospheric conditions for the periods when the cyclonic and anticyclonic flows dominate. The criterion for defining these periods was that the gyre index is in the first or fourth quartile of its range for a period of one week or longer. Other thresholds and timeframes produced qualitatively similar results. During periods of larger volume transport through the Greenland side of the array, the barrier flow through the Denmark Strait is more coastally confined, forced by a deeper low pressure center closer to the coast of Greenland (Figure 13c,e). This pressure

field also forces a region of southerly winds extending from the Irminger Sea to the west coast of Iceland and into the Denmark Strait. This flow regime results in positive wind stress curl over the Blosseville Basin, conducive for cyclonic circulation.

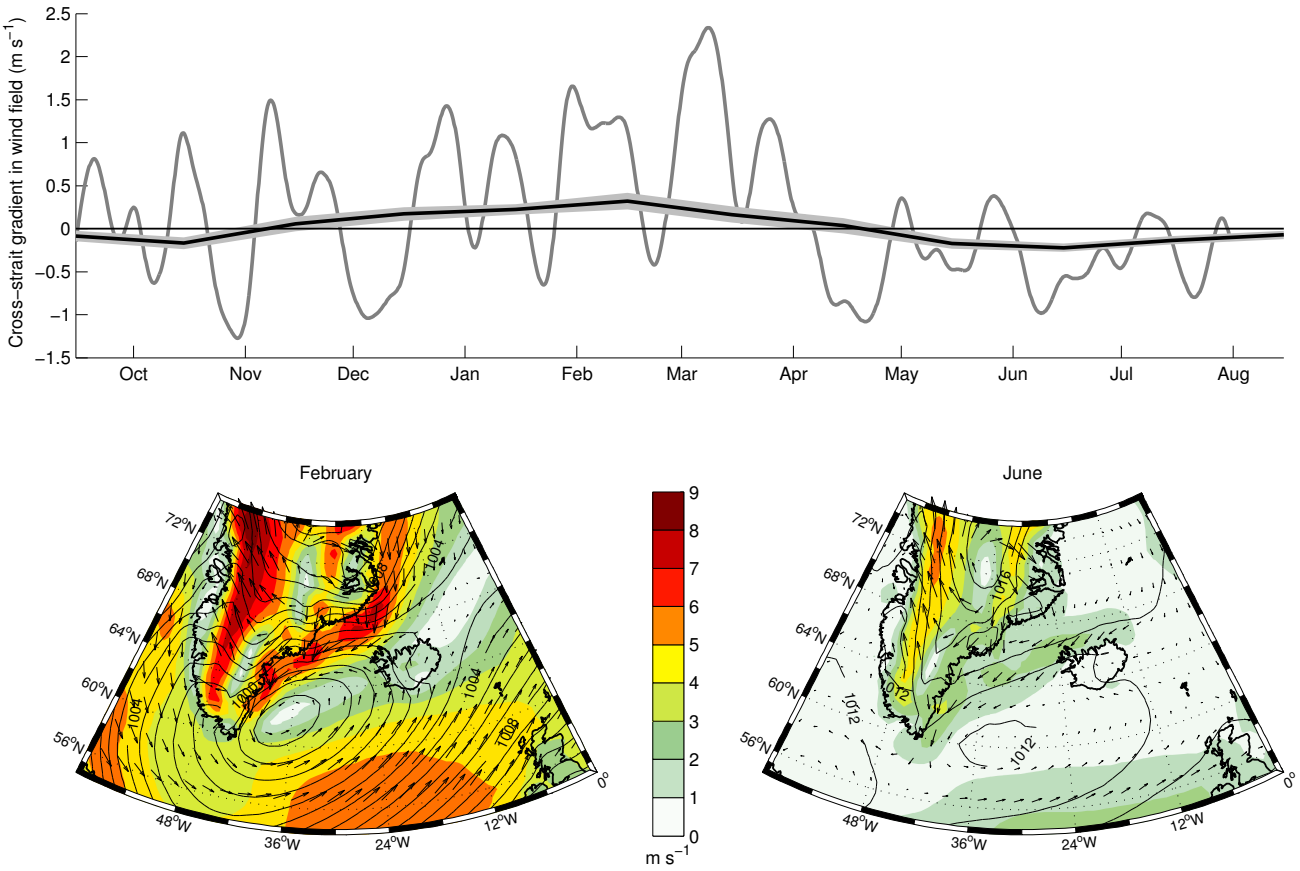

Figure 14: Top: Monthly mean climatological cross-strait gradient in along-strait wind from ERA-Interim from 1979 to 2012 (black line). The light gray shading is the standard error. Overlaid is the cross-strait gradient in wind for the year of the array, from Figure 13a (gray line). Bottom: Composite fields of 10-m vector wind speed (colors), 10-m wind vectors, and sea level pressure (contours) from the full 1979–2012 record for the two months (February and June) that have the strongest magnitude of the cross-strait gradient, but opposite sign.

The converse is true for larger transports through the Iceland side of the array (Figure 13d,f). In this case the region of barrier flow widens and extends over much of the strait due to the southeastward displacement of the composite low. This in turn results in a weakly negative wind stress curl over the

476 Blosseville Basin which is favorable for anti-cyclonic circulation. However, this atmospheric shift is
477 more subtle and there is less of a difference between the winds on the two sides of the strait, which
478 might explain the propensity for the stronger cyclonic regime in our records. Further inspection of the
479 composites reveals that it is the wind over the Iceland side of the array that changes the most between
480 the two cases. This is clearly seen in the anomaly composites, which show a strong reversal in the winds
481 adjacent to Iceland and very little change on the Greenland side (Figure 13d,f).

482 One sees in Figure 13a that the cyclonic regime dominated in the winter months, while the anti-
483 cyclonic state was more common during the remainder of the year. This begs the question of whether
484 this is a seasonal phenomenon. To address this we used the full 34-year ERA-Interim record to construct
485 a climatological cross-strait wind gradient time series (Figure 14). This reveals an annual cycle, which
486 follows the same trend as our year-long record (Figure 13a). Furthermore, the spatial composites corre-
487 sponding to the two extreme months of February and June are similar in character to the cyclonic and
488 anti-cyclonic composites presented above for the gyre index. This implies that the wind-forced partition-
489 ing of transport in the two EGC branches is potentially a seasonal feature, emphasizing the importance
490 of the atmospheric conditions in dictating how overflow water approaches the sill.

491 Finally, we composited the periods during the year when neither of the EGC branches dominated in
492 transport (not shown). This case is very similar to the record-long mean and supports our contention
493 that the cyclonic and anti-cyclonic flow regimes are distinct and significant. It is important to note that
494 the width of the Denmark Strait is only marginally resolved in the ERA-Interim product. However, the
495 broader-scale conditions are well captured and are likely to generate significantly different conditions in
496 the strait, even if the particular values and cross-strait structure in our composites are not quantitatively
497 precise.

6. Conclusions and Discussion

We have presented the initial results from a year-long densely-instrumented mooring array deployed across the northern part of Denmark Strait roughly 200 km upstream of the sill. The array spanned from the Iceland shelfbreak to the Greenland shelf and hence captured the vast majority of the Denmark Strait Overflow Water (DSOW) transport.

The year-long mean total volume transport of DSOW was 3.54 ± 0.16 Sv. This displayed a weak seasonal signal that peaked in fall and winter, and was characterized by significant synoptic variability on time scales consistent with that seen downstream at the sill (Jochumsen et al., 2012). A significant portion of the overflow comes from below sill depth (0.58 ± 0.07 Sv), indicating that there is aspiration into the plume.

We documented two distinct sources of overflow water approaching the sill whose origins were identified using historical hydrographic data. One is the warm, salty Return Atlantic Water that is found upstream of the array in the vicinity of the East Greenland shelfbreak and slope. This is the well established Nordic Seas boundary current water that enters the Blosseville Basin in the East Greenland Current, which was evident in our array as a surface intensified jet near the shelfbreak (referred to as the Shelfbreak EGC). The return Atlantic water was also present in the central part of the Blosseville Basin onto the Iceland side of the array where it is advected southward within a region of enhanced equatorward flow. We believe that this flow feature is a combination of a bifurcated branch of the East Greenland Current (referred to as the separated EGC) and the North Icelandic Jet (NIJ). According to the historical hydrography, the water advected by the NIJ, which lacks the subsurface temperature and salinity maxima of the Return Atlantic Water, corresponds to Arctic-origin water found in the central Iceland Sea.

Using a set of hydrographic criteria, we partitioned the overflow transport through the array between these two water mass sources, and found that 2.54 $\pm$ 0.17 Sv is associated with the East Greenland Current (the sum of the two branches) and 1.00 $\pm$ 0.17 Sv is due to the NIJ. In contrast to the total transport, the two components display a larger annual signal and are generally out of phase with each other; the East Greenland Current transport is seasonally larger when the NIJ transport is smaller, and vice versa. This is dictated by a combination of the location of the hydrographic boundary between the two water masses and the magnitude of the velocities.

We further partitioned the East Greenland Current into that which passes through the array on the Greenland side of the Blosseville Basin versus the Iceland side – which we interpret as the Shelfbreak EGC and the separated EGC, respectively. In the mean, the shelfbreak branch transports slightly more overflow water (1.50 $\pm$ 0.16 Sv) than the separated branch (1.04 $\pm$ 0.15 Sv). However, these two branches display considerable variability on periods longer than two weeks that are significantly anti-correlated. We argue that this is reflective of a gyre-like circulation in the Blosseville Basin that alternates between cyclonic and anti-cyclonic regimes, with the former being more prevalent. Using atmospheric reanalysis fields we demonstrated that the two regimes are associated respectively with periods of positive and negative wind stress curl over the Blosseville Basin, which in turn is strongly linked to the character of the barrier winds through the Denmark Strait. Consideration of the full 34-year reanalysis record suggests that the two regimes are seasonal – cyclonic in the winter months and (weakly) anti-cyclonic over the remainder of the year.

Our study demonstrates robustly that about a third of the DSOW approaching the sill emanates from a source other than the Nordic Seas boundary current. Given this significant contribution, it is of much interest to determine the origin and formation mechanisms of the Arctic Origin water. Våge et al. (2011b)

suggested that convection in the Iceland Sea forms the water. However, this is unclear in light of the limited wintertime data in the region (Våge et al., 2015), and also given the relatively weak meteorological forcing there (Moore et al., 2012; Harden et al., 2015).

It is also of interest to determine how the different dense water branches interact and mix with each other as they approach the sill, since this will likely help dictate the final overflow water product. It is clear from our data that the separated EGC and NIJ merge to some degree, and that this process is time dependent and complex. Further work is necessary to elucidate the structure and dynamics of each dense water branch, including the possible role of hydraulic control in the partitioning of transport between them.

Acknowledgments

The authors would like to thank the crew and technicians aboard R/V Knorr and RRS James Clark Ross for the deployment and recovery of the moored array. We also thank Carolina Nobre for help with the data management. The mooring and analysis work was supported by NSF OCE research grants OCE-0959381 and OCE-1433958, by the European Union 7th Framework Programme (FP7 2007-2013) under grant agreement n. 308299 NACLIM, and and by the Research Council of Norway through the Fram Centre Flaggship project 6606-299.

AppendixA. Gridding

Here we describe the gridded product processing for the velocity and hydrography data.

Before gridding the velocity sections, we conducted some post-processing of the ADCP data. For each mooring the data from each ADCP were combined, interpolated onto a vertical grid of 5 m and low-passed in the vertical over 20 m. The strongest tides in the array were at the M2 frequency, with a

maximum magnitude of 20 cm s^{-1} in the top 200 m of the array, mostly on the Iceland side. To remove these tides, the data were low-passed at 36 hours using a second-order Butterworth filter. However, systematic near-surface data gaps produced by diurnal migration of scatterers were partly synchronized with the tidal frequency and biased the low-pass to certain phases of the tide. To remove this effect an attempt was made to fill in some of the data near the top of ADCP records. For moorings where current meter data were available at 100 m, filling was achieved by linear interpolation to this depth. Above 100 m and for moorings with no current meter above the top-most ADCP, a linear regression was performed between deep and shallow ADCP bins for times where there was data to shallow depths. The regressions were robust in all cases ($r > 0.9$) and the linear coefficients were used to fill in data gaps. The current meter data were also detided using the same 36 hour filter. All velocity data were then passed to a gridding routine as described in the main text.

Hydrographic sections were also produced using the same gridding routine at the same resolution. However, gridding across the section proved problematic for mapping features below approximately 200 m. One issue was in joining two regions with the same Θ-S properties along steep isopycnal slopes, particularly at the depth of the subsurface salinity maximum (e.g. see Figure 5) . Gridding often generated isolated maxima instead of filaments running along isopycnals. This issue was resolved by using a density-space gridding method in the deeper part of the water column. The temperature and salinity data were first gridded in distance and density using a resolution of 8 km in the horizontal and 0.01 kg m^{-3} in the "vertical". This gridded product was then converted back into depth-space using a density section (in x and z). In order for a unique placement of temperature and salinity data back in depth-space, it was important to ensure that the gridded density section had no inversions. Therefore, the density data from each mooring were first interpolated in depth using a shape and gradient preserving spline, before being

passed to the depth-distance gridding routine. The few remaining inversions were removed manually. This gridded density section was then used to convert the salinity and temperature sections from density- to depth-space. We will refer to this process as gridding step 1. As expected, the resulting sections showed better mapping of hydrographic features along isopycnals below 200 m. However, the method worked poorly at shallow depth where there were large gradients between the properties measured by neighboring moorings. We therefore implemented a second gridding step. We used the data from gridding step 1 below the 27.9 kg m^{-3} isopycnal and then all the remaining data from above this interface to grid in depth-space once more. Examples of gridded products made through both methods can be found on the Kögur website (http://kogur.whoi.edu).

AppendixB. Transport Error Estimates

Here, we will discuss both the errors in individual transport snapshots and the error associated with computing the mean transport over the deployment period.

We start with the error in individual section transport estimates. The first source of error is from the accuracies of the velocity instrumentation, which are ± 1 cm s^{-1} for the Aquadopps and RCM-7s and ± 0.5 cm s^{-1} for all other instruments. Assuming that all errors are independent, and working out a representative area in the array that any one instrument sampled, the combined transport error from instrument accuracy was 0.17 Sv. Another source of error comes from the coarse sampling, bottom triangles and the representative area under the 27.8 kg m^{-3} isopycnal. We assessed this by down-scaling the velocity and density data to a finer grid and computed the transports again. We also computed the transport by multiplying the mean velocity by the polygonal area of the bottom and 27.8 kg m^{-3} isopycnal. In all cases, the difference in transport values produced are small, with a standard deviation of 0.09 Sv. The final source of error, and the largest, is based on the fact that the velocity records at

neighboring moorings in the central array (KGA7 – KGA9) are often uncorrelated, meaning we are only marginally capturing the synoptic field's horizontal scales and the gridding becomes less certain. We assessed this error by recalculating the transport based on a regridding that gave each mooring a larger influence on the neighboring grid points. This is the biggest source of error, at, on average, 0.41 Sv. Combining all errors, we estimate that the average error in any one section is $\pm$0.45 Sv.

In addition to these errors we also assessed the error in the individual section EGC and NIJ transports produced by the definition of the boundary. If we assume that our choice of boundary is accurate to within the grid spacing of the data (8 km) we can assess the upper and lower bounds of this data set by displacing the interface by 8 km in either direction and recalculating the transport in each branch. In this manner we calculate that the error in our division is on average $\pm$0.84 Sv. However, given that we assume this value to be stochastically applied to each estimate, the impact on the record-long mean error is minimal.

The errors that we quote in the paper are for deployment-length mean transports. The error in this value stems in part from the above error in individual estimates, but mainly from the natural variability in the system, which is significant (see Figure 10). This standard error (the accuracy of calculating a population mean from a number of finite samples) is usually assessed as the standard deviation of the sample divided by the square root of the number of samples. When dealing with a time series, the autocorrelation of individual "samples" needs to be accounted for to provide a representative number of independent samples. In our case, this is 167 (1008 data points and an autocorrelation timescale of 2 days).

Clearly, the individual section estimate error will impact the estimation of the standard error. As such, we combined these errors using a Monte Carlo approach. For a given number of samples (e.g.

167) distributed with a standard deviation about a sample mean, we added a random error based on the individual transport estimate. We then computed the theoretical standard error for this new set. Repeating this e.g. 20,000 times allows us to assess how much the individual errors in measurements affects the standard error of the distribution. We can do this for both the total transports and for the individual components. The error in the deployment-long transport mean comes out as ± 0.16 Sv. Other errors are calculate in a similar manner and are quoted in the text.

The accuracy in the transport of water that is aspired to join the overflow is limited not by temporal variability, but by our limited vertical resolution and uncertainty in the sill depth. As such, we estimate the error for this value by calculating the mean aspiration if the interface were displaced over a range of 50 m around our 650 m estimate.

Bibliography

de Steur, L., Hansen, E., Gerdes, R., Karcher, M., Fahrbach, E., Holfort, J., 2009. Freshwater fluxes in the East Greenland Current: A decade of observations. Geophysical Research Letters 36 (23), L23611, 10.1029/2009GL041278.

Dee, D. P., Uppala, S. M., Simmons, A. J., Berrisford, P., Poli, P., Kobayashi, S., Andrae, U., Balmaseda, M. A., Balsamo, G., Bauer, P., Bechtold, P., Beljaars, A. C. M., van de Berg, L., Bidlot, J., Bormann, N., Delsol, C., Dragani, R., Fuentes, M., Geer, A. J., Haimberger, L., Healy, S. B., Hersbach, H., Hólm, E. V., Isaksen, L., Kållberg, P., Köhler, M., Matricardi, M., McNally, A. P., Monge-Sanz, B. M., Morcrette, J. J., Park, B. K., Peubey, C., de Rosnay, P., Tavolato, C., Thépaut, J. N., Vitart, F., 2011. The ERA-Interim reanalysis: configuration and performance of the data assimilation system. Quarterly Journal of the Royal Meteorological Society 137 (656), 553–597, 10.1002/qj.828.

Dickson, R., Meincke, J., Rhines, P. (Eds.), 2008. Arctic–Subarctic Ocean Fluxes: Defining the Role of the Northern Seas in Climate. Springer Netherlands, 10.1007/978-1-4020-6774-7.

Dickson, R. R., Brown, J., 1994. The production of North Atlantic Deep Water: Sources, rates, and pathways. J. Geophys. Res. 99 (C6), 12319–12341, 10.1029/94JC00530.

Eldevik, T., Nilsen, J. E. Ø., Iovino, D., Anders Olsson, K., Sandø, A. B., Drange, H., 2009. Observed sources and variability of Nordic seas overflow. Nature Geosci 2 (6), 406–410, 10.1038/ngeo518.

Hansen, B., Østerhus, S., 2007. Faroe Bank Channel overflow 1995–2005. Progress in Oceanography 75 (4), 817 – 856, 10.1016/j.pocean.2007.09.004.

Harden, B. E., Pickart, R. S., Renfrew, I. A., 2014a. Offshore transport of dense water from the East Greenland shelf. Journal of Physical Oceanography 44 (1), 229–245, 10.1175/JPO-D-12-0218.1.

Harden, B. E., Renfrew, I. A., Petersen, G. N., 2011. A climatology of wintertime barrier winds off southeast Greenland. J. Climate 24 (17), 4701–4717, 10.1175/2011JCLI4113.1.

Harden, B. E., Renfrew, I. A., Petersen, G. N., 2015. Meteorological buoy observations from the central Iceland Sea. Journal of Geophysical Research: Atmospheres 120 (8), 3199–3208, 10.1002/2014JD022584.

Harden, B. E., Straneo, F., Sutherland, D. A., 2014b. Moored observations of synoptic and seasonal variability in the East Greenland Coastal Current. Journal of Geophysical Research: Oceans 119 (12), 8838–8857, 10.1002/2014JC010134.

Jochumsen, K., Quadfasel, D., Valdimarsson, H., Jónsson, S., 2012. Variability of the Denmark Strait overflow: Moored time series from 1996–2011. Journal of Geophysical Research: Oceans 117 (C12), C12003, 10.1029/2012JC008244.

Jónsson, S., Valdimarsson, H., 2004. A new path for the Denmark Strait overflow water from the Iceland Sea to Denmark Strait. Geophysical Research Letters 31 (3), L03305, 10.1029/2003GL019214.

Jónsson, S., Valdimarsson, H., 06 2012. Hydrography and circulation over the southern part of the Kolbeinsey Ridge. ICES Journal of Marine Science: Journal du Conseil.

Kinder, T. H., Parrilla, G., 1987. Yes, some of the Mediterranean outflow does come from great depth. Journal of Geophysical Research: Oceans 92 (C3), 2901–2906, 10.1029/JC092iC03p02901.

677 Köhl, A., Käse, R. H., Stammer, D., Serra, N., 2007. Causes of changes in the Denmark Strait overflow.
678 Journal of Physical Oceanography 37 (6), 1678–1696, 10.1175/JPO3080.1.

679 Macrander, A., Send, U., Valdimarsson, H., Jónsson, S., Käse, R. H., 2005. Interannual changes in the
680 overflow from the Nordic Seas into the Atlantic Ocean through Denmark Strait. Geophysical Research
681 Letters 32 (6), L06606, 10.1029/2004GL021463.

682 Mauritzen, C., 1996. Production of dense overflow waters feeding the North Atlantic across the
683 Greenland-Scotland Ridge. Part 1: Evidence for a revised circulation scheme. Deep Sea Research
684 Part I: Oceanographic Research Papers 43 (6), 769–806, 10.1016/0967-0637(96)00037-4.

685 Moore, G. W. K., Renfrew, I. A., Pickart, R. S., 2012. Spatial distribution of air-sea heat
686 fluxes over the sub-polar North Atlantic Ocean. Geophysical Research Letters 39 (18), L18806,
687 10.1029/2012GL053097.

688 National Geospatial-Intelligence Agency, 2004. Handbook of magnetic compass ad-
689 justment. Tech. rep., National Geospatial-Intelligence Agency, Bethesda, MD,
690 http://msi.nga.mil/MSISiteContent/StaticFiles/HoMCA.pdf.

691 Nikolopoulos, A., Pickart, R. S., Fratantoni, P. S., Shimada, K., Torres, D. J., Jones, E. P., Aug. 2009. The
692 western Arctic boundary current at 152°W: Structure, variability, and transport. Deep Sea Research
693 Part II: Topical Studies in Oceanography 56 (17), 1164–1181, 10.1016/j.dsr2.2008.10.014.

694 Rudels, B., Fahrbach, E., Meincke, J., Budéus, G., Eriksson, P., 2002. The East Greenland Current and
695 its contribution to the Denmark Strait overflow. ICES Journal of Marine Science: Journal du Conseil
696 59, 1133–1154, 10.1006/jmsc.2002.1284.

697 Sandø, A. B., Nilsen, J. E. Ø., Eldevik, T., Bentsen, M., 2012. Mechanisms for variable North
698 Atlantic–Nordic seas exchanges. Journal of Geophysical Research: Oceans 117 (C12), C12006,
699 10.1029/2012JC008177.

700 Smethie, W. M., Swift, J. H., 1989. The tritium:krypton-85 age of Denmark Strait Overflow Water and
701 Gibbs Fracture Zone Water just south of Denmark Strait. Journal of Geophysical Research-Oceans
702 94 (C6), 8265–8275, 10.1029/JC094iC06p08265.

703 Strass, V. H., Fahrbach, E., Schauer, U., Sellmann, L., 1993. Formation of Denmark Strait overflow
704 water by mixing in the East Greenland Current. Journal of Geophysical Research: Oceans 98 (C4),
705 6907–6919, 10.1029/92JC02732.

706 Swift, J. H., Aagaard, K., 1981. Seasonal transitions and water mass formation in the Iceland and
707 Greenland seas. Deep Sea Research Part A. Oceanographic Research Papers 28 (10), 1107–1129,
708 10.1016/0198-0149(81)90050-9.

709 Swift, J. H., Aagaard, K., Malmberg, S.-A., 1980. The contribution of the Denmark Strait overflow to
710 the deep North Atlantic. Deep Sea Research Part A. Oceanographic Research Papers 27 (1), 29–42,
711 10.1016/0198-0149(80)90070-9.

712 Tanhua, T., Bulsiewicz, K., Rhein, M., 2005. Spreading of overflow water from the Greenland to the
713 Labrador Sea. Geophysical Research Letters 32 (10), L10605, 10.1029/2005GL022700.

714 Våge, K., Moore, G. W. K., Jónsson, S., Valdimarsson, H., 2015. Water mass transformation in
715 the Iceland Sea. Deep Sea Research Part I: Oceanographic Research Papers 101 (0), 98–109,
716 10.1016/j.dsr.2015.04.001.

717 Våge, K., Pickart, R. S., Sarafanov, A., Knutsen, Ø., Mercier, H., Lherminier, P., van Aken, H. M.,
718 Meincke, J., Quadfasel, D., Bacon, S., 2011a. The Irminger Gyre: Circulation, convection, and in-
719 terannual variability. Deep Sea Research Part I: Oceanographic Research Papers 58 (5), 590–614,
720 10.1016/j.dsr.2011.03.001.

721 Våge, K., Pickart, R. S., Spall, M. A., Moore, G. W. K., Valdimarsson, H., Torres, D. J., Erofeeva, S. Y.,
722 Nilsen, J. E. Ø., 2013. Revised circulation scheme north of the Denmark Strait. Deep Sea Research
723 Part I: Oceanographic Research Papers 79 (0), 20–39, 10.1016/j.dsr.2013.05.007.

724 Våge, K., Pickart, R. S., Spall, M. A., Valdimarsson, H., Jónsson, S., Torres, D. J., Østerhus, S., Eldevik,
725 T., 2011b. Significant role of the North Icelandic Jet in the formation of Denmark Strait overflow
726 water. Nature Geosci 4 (10), 723–727, 10.1038/ngeo1234.

727 von Appen, W.-J., 2014. Structure and dynamics of high-latitude shelfbreak currents: Moored obser-
728 vations from the Beaufort Sea and the Irminger Sea. Ph.D. thesis, MIT/WHOI Joint Program, Cam-
729 bridge, MA.

730 von Appen, W.-J., Pickart, R. S., Brink, K. H., Haine, T. W. N., 2014. Water column structure and statis-
731 tics of Denmark Strait Overflow Water cyclones. Deep Sea Research Part I: Oceanographic Research
732 Papers 84, 110–126, 10.1016/j.dsr.2013.10.007.